An energy-momentum-conserving temporal discretization scheme for adhesive contact problems

Sachin S. Gautam[a] and Roger A. Sauer[1,a]

[a] *Graduate School AICES, RWTH Aachen University, Templergraben 55, 52056 Aachen, Germany*

Accepted[2] in *International Journal for Numerical Methods in Engineering*,
Submitted on 18 June 2012, Revised on 30 August 2012, Accepted on 6 September 2012

Abstract: Numerical solution of dynamic problems require accurate temporal discretization schemes. So far, to the best of authors' knowledge, none have been proposed for adhesive contact problems. In this work, an energy-momentum-conserving temporal discretization scheme for adhesive contact problems is proposed. A contact criterion is also proposed to distinguish between adhesion dominated and impact dominated contact behavior. An adhesion formulation is considered which is suitable to describe a large class of interaction mechanisms including van der Waals adhesion and cohesive zone modeling. The current formulation is frictionless and no dissipation is considered. Performance of the proposed scheme is compared with other schemes. The proposed scheme involves very little extra computational overhead. It is shown that the proposed new temporal discretization scheme leads to major accuracy gains both for single and multi degree of freedom systems. The single degree of freedom system is critically analyzed for various parameters affecting the response. For the multi degree of freedom system, the effect of the time step and mesh discretization on the solution is also studied using the proposed scheme. It is further shown that a temporal discretization scheme based on the principle of energy conservation is not sufficient to obtain a convergent solution. Results with higher order contact finite elements for discretizing the contact area are also discussed.

Keywords: adhesion, energy-momentum conserving schemes, nonlinear finite element methods, computational contact mechanics, temporal integration schemes, nonlinear dynamics

1 Introduction

Dynamic effects play an important role in engineering problems especially in the context of contact. A special class of contact problems are adhesive contact problems. Examples are thin film adhesion, surface coating, insect and lizard adhesion, rubber adhesion, MEMS, joining, bonding, and soldering. Apart from efficient contact algorithms, accurate temporal discretization schemes are required to obtain accurate numerical solutions.

Temporal discretization schemes can be classified in to two different categories: *collocation-based schemes* and *energy-momentum-conserving schemes* (Krenk, 2009). In collocation-based schemes, the equation of motion is satisfied at selected points in the time interval $[t_n, t_{n+1}]$. In contrast, for energy-momentum-conserving schemes, the equation of motion is integrated over the time interval $[t_n, t_{n+1}]$. The Newmark scheme (Newmark, 1959), which is a collocation based scheme, may induce significant errors in the numerical solution which may lead to divergence

[1] Corresponding author, email: sauer@aices.rwth-aachen.de
[2] This pdf is a personal version of an article whose final publication is available at www.onlinelibrary.wiley.com

of the numerical solution. The reason for this is that the adhesive contact behavior is highly nonlinear. Also, it is well known that even for linear systems Newmark scheme conserves energy and momentum only for a special choice of parameters. Recently, a parameter free collocation-based composite temporal discretization scheme has been proposed by Bathe (2007) with the objective to conserve energy. Alternatively, *energy-momentum-conserving schemes* have been developed with the idea of conserving properties of the underlying problem i.e., energy and momentum. The energy-momentum-conserving schemes have been applied to elastodynamics through the pioneering work of Simo and Tarnow (1992). They presented a new methodology for the construction of time integration algorithms, called energy-momentum-conserving algorithms (EMCA), that inherit, by design, the conservation laws of momentum and energy. Later, (Betsch and Steinmann, 2001) used a nonstandard quadrature formula, based on the discrete gradient method of (Gonzalez, 1996), for studying the energy conservation in nonlinear elastodynamics. Recently, Hesch and Betsch Hesch and Betsch (2009, 2010) have developed a new energy-momentum-conserving scheme by extending the discrete gradient method of Gonzalez (1996) and the one-step method of Betsch and Steinmann (2001) for contact-impact problems using the mortar finite element method.

Although a number of temporal discretization schemes have been developed for contact-impact problems (see e.g. Laursen and Love, 2002; Bravo et al., 2011), it seems, to the best of authors' knowledge, that so far none has been proposed for dynamic adhesive contact problems. Collocation-based schemes are known for the loss of conservation properties specially in the case of sudden shocks in the system. On the other hand, energy-momentum-conserving schemes have been shown to be conservative and stable. Since, the class of problems considered in the present work focuses on potential based formulations, developing an energy-momentum-conserving scheme seems to be a natural choice. The objective of the current work is to propose an energy-momentum-conserving temporal discretization scheme which is accurate and conserves energy for a conservative system. It is believed that the proposed scheme will be advantageous in the simulation of complex dynamic adhesive contact problems like the peeling of gecko spatule from rough surfaces.

The remainder of this paper is structured as follows: Section 2 provides an overview of the adhesion model used to describe the adhesive contact between deformable bodies. Section 3 first presents the weak formulation of the dynamic adhesive contact problem. Then, the finite element formulation is presented. Section 4 presents the proposed energy-momentum-conserving temporal discretization scheme for adhesive contact. In Sections 5 and 6, results of some representative numerical examples are presented. Section 7 concludes this paper.

2 Adhesion Model

2.1 Adhesion formulation

In this section, a brief overview of the adhesion formulation considered here is presented which is suitable to describe a large class of interaction mechanisms like classical contact with penalty and barrier formulations, physical interaction formulations like cohesive zone models as well as electrostatic, gravitation, and van der Waals interactions, (see Sauer and Lorenzis, 2012). The formulation is based on a Lagrangian description. According to the model, the interaction between two deformable bodies $\mathcal{B}_k$ $(k = 1, 2)$ can be described by the contact interaction energy

$$\Pi_{\mathrm{c}} = \int_{\partial\mathcal{B}_k} \beta_k^{\mathrm{s}}\, \Phi_\ell \, \mathrm{d}a_k \ , \tag{1}$$

where β_k^{s} is the current surface density at $\boldsymbol{x}_k \in \partial\mathcal{B}_k$, defined as the number of interacting particles per current surface area, and Φ_ℓ denotes the interaction potential between a particle at $\boldsymbol{x}_k$ and the neighboring body $\mathcal{B}_\ell$ ($\ell \neq k$). The potential Φ_ℓ depends on the distance, r_{s}, between $\boldsymbol{x}_k$ and surface $\partial\mathcal{B}_\ell$. Here, we consider the number of surface particles to be conserved during deformation such that

$$\beta_k^{\mathrm{s}}\,\mathrm{d}a_k = \beta_{0k}^{\mathrm{s}}\,\mathrm{d}A_k = \text{const.} \tag{2}$$

where β_{0k}^{s} is the reference surface density and $\mathrm{d}A_k$ is the reference area. This assumption is reasonable for solids. The variation of Π_{c}, due to variations of the configuration $\boldsymbol{x}_k = \boldsymbol{\varphi}_k(\boldsymbol{X}_k)$, denoted $\delta\boldsymbol{\varphi}_k$, now becomes

$$\delta\Pi_{\mathrm{c},\,k} = \int_{\partial\mathcal{B}_{0k}} \beta_{0k}^{\mathrm{s}}\,\frac{\partial\Phi_\ell}{\partial\boldsymbol{x}_k}\cdot\delta\boldsymbol{\varphi}_k\,\mathrm{d}A_k\ . \tag{3}$$

In this equation, we can identify the interaction force

$$\boldsymbol{F}_k := -\frac{\partial\Phi_\ell}{\partial\boldsymbol{x}_k} = -\frac{\partial\Phi_\ell}{\partial r_{\mathrm{s}}}\boldsymbol{n}_{\mathrm{p}}\ , \tag{4}$$

acting at $\boldsymbol{x}_k$ where r_{s} denotes the signed distance between point $\boldsymbol{x}_k \in \partial\mathcal{B}_k$ and surface $\partial\mathcal{B}_\ell$, i.e.,

$$r_{\mathrm{s}}(\boldsymbol{x}_k) := (\boldsymbol{x}_k - \boldsymbol{x}_{\mathrm{p}})\cdot\boldsymbol{n}_{\mathrm{p}}\ , \tag{5}$$

where $\boldsymbol{x}_{\mathrm{p}} \in \partial\mathcal{B}_\ell$ and $\boldsymbol{n}_{\mathrm{p}}$ denotes the position of closest projection point of $\boldsymbol{x}_k$ on $\partial\mathcal{B}_\ell$. The current surface traction

$$\boldsymbol{t}_k = \beta_k^{\mathrm{s}}\,\boldsymbol{F}_k\ , \tag{6}$$

acting on $\mathrm{d}a_k$, and the reference surface traction

$$\boldsymbol{T}_k = \beta_{0k}^{\mathrm{s}}\,\boldsymbol{F}_k\ , \tag{7}$$

that corresponds to the scaling of $\boldsymbol{t}_k$ by the area change $\mathrm{d}a_k/\mathrm{d}A_k$. As mentioned at the beginning of the section, for suitable definitions of Φ_ℓ, one can consider various contact formulations (Sauer and Lorenzis, 2012). In this paper, we focus on two cases, van der Waals adhesion and cohesive zone models. For van der Waals adhesion (Israelachvili, 1991), we have

$$\Phi_\ell := \frac{\Phi_0}{J_{s\ell}}\left[\frac{1}{360}\left(\frac{r_0}{r_{\mathrm{s}}}\right)^8 - \frac{1}{6}\left(\frac{r_0}{r_{\mathrm{s}}}\right)^2\right]\ , \qquad r_{\mathrm{s}} > 0\ , \tag{8}$$

Here, Φ_0 and r_0 are model constants and $J_{s\ell} = \mathrm{d}a_k/\mathrm{d}A_k = \beta_{0k}^{\mathrm{s}}/\beta_k^{\mathrm{s}}$ characterizes the surface deformation. This expression can also be derived from the Lennard Jones potential

$$\phi(r) = \epsilon\left(\frac{r_0}{r}\right)^{12} - 2\epsilon\left(\frac{r_0}{r}\right)^6\ , \qquad r = ||\boldsymbol{x}_1 - \boldsymbol{x}_2||\ , \tag{9}$$

between the points $\boldsymbol{x}_1 \in \mathcal{B}_1$ and $\boldsymbol{x}_2 \in \mathcal{B}_2$, (see Sauer and Wriggers, 2009). Here, ϵ is an energy parameter. Parameter r_0 denotes the equilibrium distance of the Lennard Jones potential.

Secondly, we consider the exponential cohesive zone model

$$\Phi_\ell := -\Phi_0\left(1 + \frac{r_{\mathrm{s}}}{r_0}\right)\exp\left(1 - \frac{r_{\mathrm{s}}}{r_0}\right)\ , \qquad r_{\mathrm{s}} \in \mathbb{R}\ , \tag{10}$$

(Sauer and Lorenzis, 2012), to describe mode I de-cohesion. Here, r_0 is the parameter of the model. This formulation is a special case of the Xu-Needleman model (Xu and Needleman, 1993). Models (8), (9), and (10) are used in the examples of sections 5 and 6. In the present work, only frictionless normal contact is considered. It should be noted that, in theory, these potentials and hence, the interaction forces, are smooth functions of distance and time. However, when the domain is discretized spatially and temporally, these functions can appear as non-smooth functions. The non-smoothness of the function will depend on the spatial and temporal discretization. An adaptive spatial or temporal discretization is then required for smooth behavior approximation.

2.2 Impact-adhesion criterion

For the classification of dynamic adhesive contact problems, we distinguish between adhesion dominated and impact dominated problems. For example, a body hitting a wall at large velocities is typically dominated by the impact behavior, while the peeling of an adhering strip, on the other hand, is typically dominated by the adhesion behavior. Formally, we base this distinction on the extreme values of the contact energy that are attained during contact interaction.

Let us first consider a single point $\boldsymbol{x}_k$ interacting with body $\mathcal{B}_\ell$. The interaction force $\boldsymbol{F}_k$ acting at $\boldsymbol{x}_k$, according to Eq. (8) or (10), is shown schematically in Fig. (1). Let us now consider

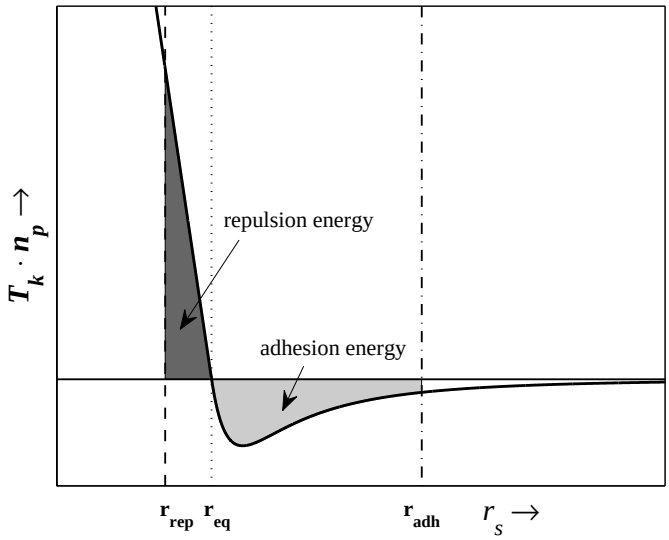

Figure 1: Schematic plot of the traction-separation behavior according to models given by Eqs. (8) and (10).

an interaction process over time t, where the distance between $\boldsymbol{x}_k$ and $\partial\mathcal{B}_\ell$ ranges between the extreme distances $r_{\text{rep}} < r_{\text{eq}}$ and $r_{\text{adh}} > r_{\text{eq}}$, i.e.,

$$r_{\text{adh}} := \max_{\forall t} r_{\text{s}} \ , \tag{11}$$

$$r_{\text{rep}} := \min_{\forall t} r_{\text{s}} \ , \tag{12}$$

as is shown in Fig. (1). Here, r_{eq} is the distance at which there is no traction acting at a point. We can then compute the maximum adhesion energy and maximum repulsion energy that is attained during the process as

$$\begin{aligned} \Phi_\ell^{\text{adh}}(\boldsymbol{x}_k) &:= \int_{r_{\text{adh}}}^{r_{\text{eq}}} \boldsymbol{F}_k \cdot \boldsymbol{n}_{\text{p}} \, \mathrm{d}r_{\text{s}} = \Phi_\ell(r_{\text{adh}}) - \Phi_\ell(r_{\text{eq}}) \ , \\ \Phi_\ell^{\text{rep}}(\boldsymbol{x}_k) &:= \int_{r_{\text{rep}}}^{r_{\text{eq}}} \boldsymbol{F}_k \cdot \boldsymbol{n}_{\text{p}} \, \mathrm{d}r_{\text{s}} = \Phi_\ell(r_{\text{rep}}) - \Phi_\ell(r_{\text{eq}}) \ , \end{aligned} \tag{13}$$

where the signs are chosen such that $\Phi_\ell^{\text{adh}} > 0$ and $\Phi_\ell^{\text{rep}} > 0$. With this we define the following classification for the behavior of point $\boldsymbol{x}_k$:

$$\begin{aligned} \Phi_\ell^{\text{adh}} > \Phi_\ell^{\text{rep}} &: \text{ adhesion dominated problem,} \\ \Phi_\ell^{\text{adh}} < \Phi_\ell^{\text{rep}} &: \text{ impact dominated problem.} \end{aligned} \tag{14}$$

Remarks:

1. In case $\Phi_\ell^{\text{adh}} \ll \Phi_\ell^{\text{rep}}$, the behavior corresponds to that of a classical contact problem without adhesion. Formulations (8) and (10) can then be viewed as a regularized penalty formulation.

2. If Φ_ℓ is the only potential energy in the system, and no dissipation is considered, we have $\Phi_\ell^{\text{adh}} = \Phi_\ell^{\text{rep}}$. This is considered in some of the examples shown in section 5.

3. If additional potential energy, e.g., strain energy, is present in the system, it may substantially exceed both Φ_ℓ^{adh} and Φ_ℓ^{rep} during interaction. In this case the problem is neither dominated by adhesion nor impact, since the contact interaction becomes insignificant. Examples are shown in section 5.

Classification (14) can be extended to interacting bodies, if we consider the integration

$$\begin{aligned} \Pi_{\text{c}}^{\text{adh}} &:= \int_{\partial\mathcal{B}_k} \beta_k^{\text{s}}\, \Phi_\ell^{\text{adh}}(\boldsymbol{x}_k)\, \text{d}a_k \ , \\ \Pi_{\text{c}}^{\text{rep}} &:= \int_{\partial\mathcal{B}_k} \beta_k^{\text{s}}\, \Phi_\ell^{\text{rep}}(\boldsymbol{x}_k)\, \text{d}a_k \ . \end{aligned} \tag{15}$$

in analogy to Eq. (1). It should be noted that, in general, both Φ_ℓ^{adh} and Φ_ℓ^{rep}, due to Eqs. (11) and (12), are attained at different instances in time across $\partial\mathcal{B}_k$. Hence, the integrals of Eq. (15) are not carried out at the same instance in time. The quantities $\Pi_{\text{c}}^{\text{adh}}$ and $\Pi_{\text{c}}^{\text{adh}}$ are therefore measures that characterize adhesion and impact behavior of $\mathcal{B}_k$ during a given contact interaction process. The behavior of body $\mathcal{B}_k$ can then be classified in analogy to Eq. (14) now using $\Pi_{\text{c}}^{\text{adh}}$ and $\Pi_{\text{c}}^{\text{rep}}$. The remarks given above extend correspondingly, see also appendix A.

3 Weak Formulation and Finite Element Discretization

In this section, we outline the weak form for the dynamic interaction between two general continua $\mathcal{B}_1$ and $\mathcal{B}_2$ and also present the finite element formulation. The Lagrangian of the system, L, is given by

$$L \ = \ K \ - \ \Pi \ , \tag{16}$$

where

$$K \ = \ \sum_{k=1}^{2} K_k \ = \ \sum_{k=1}^{2} \frac{1}{2} \int_{\mathcal{B}_k} \rho_k \boldsymbol{v}_k \cdot \boldsymbol{v}_k \, \text{d}v_k \tag{17}$$

is the kinetic energy of the two-body system with $\boldsymbol{v}_k = \dot{\boldsymbol{x}}_k$ and ρ_k is the current density. The potential energy, Π, is given by

$$\Pi \ = \ \Pi_{\text{int}} \ + \ \Pi_{\text{c}} \ - \ \Pi_{\text{ext}} \ , \tag{18}$$

where $\Pi_{\text{int}} \ = \ \sum_{k=1}^{2} \Pi_{\text{int},k}$ is the internal energy of the system with $\Pi_{\text{int},k} \ = \ \int_{\mathcal{B}_{0k}} W_k \text{d}V_k$. Here, W_k is a scalar-valued strain energy density function and Π_{ext} is the external energy of the system. The contact energy Π_{c} is given by Eq. (1). In the problems considered in the present work, $\Pi_{\text{ext}} \ = \ 0$. From Eq. (16), weak form for the dynamic problem can be derived as

$$\sum_{k=1}^{2} \left[\int_{\mathcal{B}_k} \delta\boldsymbol{\varphi}_k \cdot \rho_k \ddot{\boldsymbol{x}}_k \, \text{d}v_k \ + \ \int_{\mathcal{B}_k} \text{grad}\,(\delta\boldsymbol{\varphi}_k) : \boldsymbol{\sigma}_k \, \text{d}v_k \ - \ \int_{\partial\mathcal{B}_k} \delta\boldsymbol{\varphi}_k \cdot \boldsymbol{t}_k \, \text{d}a_k \right] \ = \ 0 \ , \forall\, \delta\boldsymbol{\varphi}_k \ \in \ \mathcal{V}_k \ , \tag{19}$$

where $\mathcal{V}_k$ is the space of kinematically admissible variations of deformation $\boldsymbol{\varphi}_k$, (see references Sauer, 2006; Sauer and Li, 2007) for details. In the weak form (Eq. 19), the Cauchy stress tensor $\boldsymbol{\sigma}_k$ in $\mathcal{B}_k$ is obtained from a constitutive model like a hyperelastic model. In this work, a particular form of a hyperelastic model i.e., the Neo-Hookean material model (Zienkiewicz and Taylor, 2005), given by

$$W = \frac{\mu}{2}\left(\mathrm{tr}\boldsymbol{B} - 3\right) - \mu \ln J + \frac{\Lambda}{2}\left(\ln J\right)^2 \ , \tag{20}$$

has been considered. Here, $\boldsymbol{B}$ is the left Cauchy-Green tensor and $J = \sqrt{\det \boldsymbol{B}}$. In the above expression, μ and Λ are the Lamé constants.

Next, we present the finite element formulation for the weak form corresponding to Eq. (19). We consider a displacement-based finite element description. The domains $\mathcal{B}_k$ and $\partial\mathcal{B}_k$ are partitioned into volume elements Ω_k^e and surface elements Γ_k^e each containing n_n nodes. For the volume element Ω_k^e, $n_n = n_{ve}$ and for the surface element Γ_k^e, $n_n = n_{se}$. Within each element, the displacement field $\boldsymbol{u}$ and the variations $\delta\boldsymbol{\varphi}$ are approximated by the interpolations

$$\boldsymbol{u} \approx \mathbf{N}_e \mathbf{u}^e \ , \qquad\qquad \delta\boldsymbol{\varphi} \approx \mathbf{N}_e \mathbf{w}^e \ , \tag{21}$$

where $\mathbf{u}^e$ and $\mathbf{w}^e$ denote the displacement and variations of the nodes of element e and the matrix $\mathbf{N}_e$ is given as

$$\mathbf{N}_e = \left[N_1\mathbf{I},\, N_2\mathbf{I}, \ldots,\, N_{n_n}\mathbf{I}\right] \ , \tag{22}$$

which is a $[n_{\mathrm{dim}} \times (n_{\mathrm{dim}} \cdot n_n)]$ matrix formed by the n_n shape functions $N_I\,(I = 1, 2, \ldots, n_n)$ of the element. Here, $n_{\mathrm{dim}} \leq 3$ is the dimension of the Euclidean space occupied by the reference configuration of the solid body Ω_{0k}^e and $\mathbf{I}$ is an identity matrix of size $(n_{\mathrm{dim}} \times n_{\mathrm{dim}})$. Inserting approximations (21) into the weak form (19) and assembly over all the volume and surface elements leads to

$$\mathbf{w}^T\left[\mathbf{M}\mathbf{a} + \mathbf{f}_{\mathrm{int}} + \mathbf{f}_{\mathrm{c}}\right] = \mathbf{0} \ , \qquad \forall\, \mathbf{w} \in \mathcal{V}^h \ , \tag{23}$$

where $\mathcal{V}^h$ is the space of admissible nodal displacements, $\mathbf{M}$ is the globally assembled consistent mass matrix, $\mathbf{a}$ $(= \ddot{\mathbf{u}})$ is the globally assembled acceleration vector and $\mathbf{f}_{\mathrm{int}}$ and $\mathbf{f}_{\mathrm{c}}$ are the globally assembled internal and contact force vectors. These vectors are assembled from the elemental vectors $\mathbf{f}_{\mathrm{int},k}^e$ and $\mathbf{f}_{\mathrm{c},k}^e$. The internal force vector $\mathbf{f}_{\mathrm{int},k}^e$ acting on the n_{ve} volume nodes of the volume element Ω_k^e and the elemental contact force vector $\mathbf{f}_{\mathrm{c},k}^e$ acting on the n_{se} surface nodes of the surface element Γ_k^e, and the elemental mass matrix $\mathbf{M}_k^e$ are given as

$$\mathbf{f}_{\mathrm{int},k}^e = \int_{\Omega_k^e} \mathbf{B}_e^T \boldsymbol{\sigma}_k^e \mathrm{d}v_k \ , \tag{24}$$

$$\mathbf{f}_{\mathrm{c},k}^e = -\int_{\Gamma_k^e} \mathbf{N}_e^T \boldsymbol{t}_k \mathrm{d}a_k = -\int_{\Gamma_{0k}^e} \mathbf{N}_e^T \boldsymbol{T}_k \mathrm{d}A_k \ , \tag{25}$$

$$\mathbf{M}_k^e = \int_{\Omega_k^e} \rho_k \mathbf{N}_e^T \mathbf{N}_e \mathrm{d}v_k \ , \tag{26}$$

where $\mathbf{B}_e$ is an array that contains the derivatives of the nodal shape functions N_I. Guidelines on practical implementation of Eqs. (24) - (26) can be found in finite element textbooks, (see eg. Wriggers, 2008). In the present work, damping is not considered. However, it can be included by considering dissipative material behavior or in an ad hoc manner, e.g. by using Rayleigh damping.

4 Energy-Momentum-Conserving Temporal Discretization Scheme

A system of second-order ordinary differential equations are obtained from Eq. (23) after noting that the variations $\mathbf{w}$ are arbitrary. The equations are then written at time $t = t_{n+1}$ as

$$\mathbf{M}\mathbf{a}^{n+1} + \mathbf{f}_{\text{int}}^{n+1} + \mathbf{f}_{\text{c}}^{n+1} = \mathbf{0} \,. \tag{27}$$

Given the displacement $\mathbf{u}^n$, velocity $\mathbf{v}^n$ and acceleration $\mathbf{a}^n$ at time $t = t_n$, the objective now is to find $\mathbf{u}^{n+1}$, $\mathbf{v}^{n+1}$ and $\mathbf{a}^{n+1}$ at time $t = t_{n+1}$. In the present work, we focus on an energy-momentum-conserving implicit scheme proposed by Betsch and Steinmann (2001) as it exploits the potential formulation of the system to enforce the conservation of energy and momentum. Extending the linear time finite element formulation[3] of Betsch and Steinmann (2001) by incorporating adhesive contact, the general time finite element equations can be written as

$$\mathbf{x}^{n+1} - \mathbf{x}^n - \frac{\Delta t}{2}\mathbf{M}^{-1}\cdot\left(\mathbf{p}^{n+1} + \mathbf{p}^n\right) = \mathbf{0} \,, \tag{28}$$

$$\mathbf{p}^{n+1} - \mathbf{p}^n + \int_{t_n}^{t_{n+1}} \left(\mathbf{f}_{\text{int}} + \mathbf{f}_{\text{c}}\right) \mathrm{d}t = \mathbf{0} \,, \tag{29}$$

where $\mathbf{x}^{n+1}$ and $\mathbf{x}^n$ are the coordinate vectors, and $\mathbf{p}^{n+1}$ $\left(= \mathbf{M}\mathbf{v}^{n+1}\right)$ and $\mathbf{p}^n$ $(= \mathbf{M}\mathbf{v}^n)$ are the momentum vectors at time t_{n+1} and t_n respectively. The update for the velocity can be derived from Eq. (28) as

$$\mathbf{v}^{n+1} = \frac{2}{\Delta t}\left(\mathbf{x}^{n+1} - \mathbf{x}^n\right) - \mathbf{v}^n \,, \tag{30}$$

To facilitate further derivations, the time finite element in the time interval $\mathcal{T} \in [t_n, t_{n+1}]$ is mapped to a master element with local coordinate $\alpha \in [0, 1]$ where $\alpha(t) = (t - t_n)/\Delta t$ with $\Delta t = (t_{n+1} - t_n)$. Further, Eqs. (28) and (29) are expressed for each node J ($J = 1, 2, \ldots, n_{\text{node}}$ where n_{node} are total nodes). Then, we obtain

$$\mathbf{x}_J^{n+1} - \mathbf{x}_J^n - \frac{\Delta t}{2}\sum_{K=1}^{n_{\text{node}}} \mathbf{M}_{JK}^{-1}\left(\mathbf{p}_K^{n+1} + \mathbf{p}_K^n\right) = \mathbf{0} \,, \tag{31}$$

$$\mathbf{p}_J^{n+1} - \mathbf{p}_J^n + \Delta t \int_0^1 \left(\mathbf{f}_{\text{int}}^J + \mathbf{f}_{\text{c}}^J\right) \mathrm{d}\alpha = \mathbf{0} \,, \tag{32}$$

where $\mathbf{M}_{JK}$ are the submatrices of the consistent mass matrix $\mathbf{M}$ associated with nodes J and K. The solution procedure is discussed next. Substitution for $\mathbf{p}_J^{n+1}$ from Eq. (31) in Eq. (32), the residual momentum vector $\mathbf{p}_{\text{res},J}^{n+1}$ is obtained as

$$\mathbf{p}_{\text{res},J}^{n+1}\left(\mathbf{x}_K^{n+1}\right) = \frac{2}{\Delta t}\sum_{K=1}^{n_{\text{node}}} \mathbf{M}_{JK}\left(\mathbf{x}_K^{n+1} - \mathbf{x}_K^n\right) - 2\,\mathbf{p}_J^n + \Delta t \int_0^1 \left(\mathbf{f}_{\text{int}}^J + \mathbf{f}_{\text{c}}^J\right) \mathrm{d}\alpha = \mathbf{0} \,, \tag{33}$$

with $J = 1, 2, \ldots, n_{\text{node}}$. Now, $\mathbf{p}_{\text{res},J}^{n+1}\left(\mathbf{x}_K^{n+1}\right)$ is a system of nonlinear algebraic equations which can be solved using Newton-Raphson method after assembly over all the nodes. The corresponding tangent matrix for node J needed for Newton-Raphson iterations is expressed as

$$\mathbf{L}_{JK}^{n+1} := \frac{\partial \mathbf{p}_{\text{res},J}^{n+1}}{\partial \mathbf{x}_K^{n+1}} = \frac{2}{\Delta t}\mathbf{M}_{JK} + \Delta t \frac{\partial}{\partial \mathbf{x}_K^{n+1}}\left[\int_0^1 \left(\mathbf{f}_{\text{int}}^J + \mathbf{f}_{\text{c}}^J\right) \mathrm{d}\alpha\right] \,. \tag{34}$$

[3] In the present work, we focus on the linear time finite element method. However, the derivations that follow can be easily extended to higher order time finite element methods.

It is pointed out that the conservation of linear momentum is enforced automatically through Eq. (33). As discussed in Betsch and Steinmann (2001), for the scheme to have the underlying conservation properties of the continuum system, an applicable quadrature rule needs to satisfy certain conditions. Since, the balance of linear momentum is already ensured though Eq. (33), we next focus on derivation of conditions enforced by the requirement for conservation of angular momentum and energy on the quadrature rule. These conditions in turn restrict the number of quadrature rules that can be applied.

4.1 Condition for algorithmic conservation of angular momentum

In the present work, the condition for algorithmic conservation of angular momentum in Betsch and Steinmann (2001) is extended to take into account adhesive contact. The total angular momentum, $\mathbf{G}_{n+1}$, about the origin at time t_{n+1} is expressed as

$$\mathbf{G}_{n+1} \;=\; \sum_{J=1}^{n_{\text{node}}} \mathbf{x}_J^{n+1} \times \mathbf{p}_J^{n+1} \;. \tag{35}$$

Substituting for $\mathbf{x}_J^{n+1}$ and $\mathbf{p}_J^{n+1}$ from Eqs. (31) and (32) and noting that $\mathbf{G}_n \;=\; \sum_{J=1}^{n_{\text{node}}} \mathbf{x}_J^n \times \mathbf{p}_J^n$, the condition for algorithmic conservation of angular momentum follows as

$$\mathbf{G}_{n+1} \;=\; \mathbf{G}_n \;-\; \Delta t \sum_{J=1}^{n_{\text{node}}} \mathbf{x}_m^J \times \int_0^1 \left(\mathbf{f}_{\text{int}}^J \;+\; \mathbf{f}_{\text{c}}^J\right) \mathrm{d}\alpha \;, \tag{36}$$

where $\mathbf{x}_m^J \;=\; \left(\mathbf{x}_J^{n+1} \;+\; \mathbf{x}_J^n\right)/2$. Hence, for angular momentum to be conserved i.e., $\mathbf{G}_{n+1} \;=\; \mathbf{G}_n$, the condition

$$\sum_{J=1}^{n_{\text{node}}} \int_0^1 \left(\mathbf{f}_{\text{int}}^J \;+\; \mathbf{f}_{\text{c}}^J\right) \mathrm{d}\alpha \times \mathbf{x}_m^J \;=\; \mathbf{0} \;, \tag{37}$$

should be satisfied. It can be seen that for angular momentum to be conserved, the integrals should be evaluated *exactly*. Thus, the conservation of angular momentum depends on the quadrature rule employed to evaluate the time integrals. One choice, for example, can be standard Gauss quadrature similar to that applied for evaluating the components emanating from the spatial discretization. The effect of using standard Gauss quadrature is studied later in sections (5) and (6). Note, however, that the Gauss quadrature may not be exact and hence, the angular momentum may not be conserved exactly. Thus, Eq. (37) limits the number of applicable quadrature rules for evaluating $\int_0^1 \left(\mathbf{f}_{\text{int}}^J \;+\; \mathbf{f}_{\text{c}}^J\right) \mathrm{d}\alpha$.

4.2 Condition for algorithmic energy conservation

Next, we derive the condition imposed on the applied quadrature emanating from the condition of algorithmic energy conservation. We derive the condition for the contact part. For the derivation of condition corresponding to the internal force we refer to Betsch and Steinmann (2001). Again, the time finite element formulation, corresponding to linear time finite element, after considering the adhesive contact implies that (Betsch and Steinmann, 2001)

$$\int_0^1 \left(\mathbf{f}_{\text{int}} \;+\; \mathbf{f}_{\text{c}}\right) \mathrm{d}\alpha \cdot \Delta\mathbf{x} \;+\; \mathbf{M}^{-1} \int_0^1 \mathbf{p} \mathrm{d}\alpha \cdot \Delta\mathbf{p} \;=\; 0 \;. \tag{38}$$

where $\Delta\mathbf{x} \;=\; \mathbf{x}^{n+1} \;-\; \mathbf{x}^n$ and $\Delta\mathbf{p} \;=\; \mathbf{p}^{n+1} \;-\; \mathbf{p}^n$. It can be shown (Betsch and Steinmann, 2001) that the second integral in Eq. (38) can be expressed as

$$\int_0^1 \frac{\mathrm{d}}{\mathrm{d}\alpha} \left[\frac{1}{2} \mathbf{p} \cdot \mathbf{M}^{-1} \mathbf{p}\right] \mathrm{d}\alpha \;=\; K_{n+1}^h \;-\; K_n^h \;, \tag{39}$$

where K^h_{n+1} and K^h_n denote the kinetic energy at time t_{n+1} and t_n respectively[4]. Hence, for algorithmic energy conservation the quadrature rule should fulfill the following condition

$$\int_0^1 (\mathbf{f}_{\text{int}} + \mathbf{f}_{\text{c}})\, \mathrm{d}\alpha \cdot \Delta\mathbf{x} = \Pi^{h,n+1}_{\text{int}} + \Pi^{h,n+1}_{\text{c}} - \Pi^{h,n}_{\text{int}} - \Pi^{h,n}_{\text{c}} \,, \tag{40}$$

where $\Pi^{h,n+1}_{\text{int}}$ and $\Pi^{h,n}_{\text{int}}$ denote the total strain energy and $\Pi^{h,n+1}_{\text{c}}$ and $\Pi^{h,n}_{\text{c}}$ denote the contact energy at time t_{n+1} and t_n respectively. We note that, in the present work, the contact force $\mathbf{f}_{\text{c}}$ given by Eq. (25) depends on $\boldsymbol{t}_k$ which from Eqs. (4) and (8) depends on distance r_{s}. Hence, it does not depend on the internal force $\mathbf{f}_{\text{int}}$. Also, the internal energy Π^h_{int} and the contact energy Π^h_{c} do not depend on each other. Following this observation, the expression (40) should now hold independently for internal and contact contributions. Next, the condition for the algorithmic energy conservation given by Eq. (40) is used to derive an exact expression in-terms of contact traction $\boldsymbol{T}_k$ and interaction potential Φ_ℓ. Now, in the case of a system with no internal energy Eq.(40) reduces to

$$\Pi^{h,n+1}_{\text{c}} - \Pi^{h,n}_{\text{c}} - \int_0^1 \mathbf{f}_{\text{c}}\, \mathrm{d}\alpha \cdot \Delta\mathbf{x} = 0 \,. \tag{41}$$

It can be seen that energy can be conserved only when the integral $\int_0^1 \mathbf{f}_{\text{c}}\, \mathrm{d}\alpha$ is evaluated *exactly*. Using Eqs. (1) and (2) in Eq. (41) and taking the integral outside the summation, we get the corresponding local statement as

$$\beta^s_{0k} \left[\Phi_\ell\left(\boldsymbol{x}^{n+1}_k\right) - \Phi_\ell\left(\boldsymbol{x}^n_k\right)\right] + \int_0^1 \boldsymbol{T}_k\, \mathrm{d}\alpha \cdot \Delta\boldsymbol{x}_k = 0 \,, \tag{42}$$

where $\Delta\boldsymbol{x}_k = \boldsymbol{x}^{n+1}_k - \boldsymbol{x}^n_k$. This is the condition which the quadrature rule employed should satisfy in order to algorithmically conserve contact energy and hence, the total energy of the system. One obvious choice for integration is the standard Gaussian quadrature rule that can be easily used for the computation of the time integrals. However, we consider an alternative approach which exactly fulfills the algorithmic energy and momentum conservation condition. This approach is based on the concept of the discrete gradient (Gonzalez, 1996). First, the integral $\int_0^1 \boldsymbol{T}_k\, \mathrm{d}\alpha$ in Eq. (42) can be rewritten using, Eqs. (4) and (7), as

$$\int_0^1 \boldsymbol{T}_k\, \mathrm{d}\alpha = -\beta^s_{0k} \int_0^1 \frac{\partial \Phi_\ell}{\partial \boldsymbol{x}_k}\, \mathrm{d}\alpha \,. \tag{43}$$

The current formulation is written for two deforming bodies. In this general case, the interaction potentials Φ_1 and Φ_2 are often approximated. This can lead to a loss of momentum conservation. This will be investigated in future work. In the remaining cases, we focus on interaction with rigid surfaces. The discrete gradient (Gonzalez, 1996) corresponding to the integral $-\int_0^1 \frac{\partial \Phi_\ell}{\partial \mathbf{x}_k}\, \mathrm{d}\alpha$ is proposed as

$$\begin{aligned} -\int_0^1 \frac{\partial \Phi_\ell}{\partial \boldsymbol{x}_k}\, \mathrm{d}\alpha \quad &:= \quad \overline{\nabla}\Phi_\ell \\ &:= \quad (-\mathbf{I} + \Delta\bar{\boldsymbol{x}}_k \otimes \Delta\bar{\boldsymbol{x}}_k)\, \mathrm{D}\Phi_\ell\left(\boldsymbol{x}_m\right) + \frac{-\Phi_\ell\left(\boldsymbol{x}^{n+1}_k\right) + \Phi_\ell\left(\boldsymbol{x}^n_k\right)}{\|\Delta\boldsymbol{x}_k\|}\Delta\bar{\boldsymbol{x}}_k, \end{aligned} \tag{44}$$

where $\Delta\bar{\boldsymbol{x}}_k = \Delta\boldsymbol{x}_k / \|\Delta\boldsymbol{x}_k\|$, $\mathbf{I}$ is the identity matrix and $\boldsymbol{x}_m = \left(\boldsymbol{x}^{n+1}_k + \boldsymbol{x}^n_k\right)/2$. Here, $\mathrm{D}\left(\bullet\right)$ denotes $\partial\left(\bullet\right)/\partial\boldsymbol{x}_k$. Substitution of Eq. (44) in Eq. (42) shows that the algorithmic contact

[4]The superscript h is used to signify that the values correspond to discrete system.

energy is conserved. Hence, the expression for the time integral corresponding to contact force in Eq. (33) can be written as

$$\int_0^1 \mathbf{f}_{\mathrm{c}}\,\mathrm{d}\alpha \;=\; \sum_{e=1}^{n_e}\int_0^1 \mathbf{f}^e_{\mathrm{c},k}\,\mathrm{d}\alpha \;=\; \sum_{e=1}^{n_e}\int_{\Gamma^e_{0k}} \beta^s_{0k}\mathbf{N}_e^T\,\overline{\nabla}\Phi_\ell\,\mathrm{d}A_k\;. \tag{45}$$

The time integrals in Eqs. (33) and (34) can be computed using either standard Gaussian quadrature or by employing a nonstandard quadrature rule like the discrete gradient method (Betsch and Steinmann, 2001). The formulation for the integral of the internal force has been discussed in Betsch and Steinmann (2001) and hence, is skipped. We next focus on the contact part arising from the adhesive contact potential. The finite element tangent matrix corresponding to the discrete gradient proposed in Eq. (44) is given by

$$\mathbf{L}_{\mathrm{c}}^{n+1} \;=\; \sum_{e=1}^{n_e}\mathbf{L}_{\mathrm{c}}^{e,n+1}\;,\qquad \text{where}\qquad \mathbf{L}_{\mathrm{c}}^{e,n+1} \;=\; \frac{\partial}{\partial \mathbf{u}^{e,n+1}}\left(\int_0^1 \mathbf{f}^e_{\mathrm{c},k}\,\mathrm{d}\alpha\right)\;. \tag{46}$$

Using Eq. (25), we can write

$$\mathbf{L}_{\mathrm{c}}^{e,n+1} \;=\; -\int_{\Gamma^e_{0k}} \mathbf{N}_e^T\frac{\partial}{\partial \boldsymbol{x}_k^{n+1}}\left(\int_0^1 \boldsymbol{T}_k\,\mathrm{d}\alpha\right)\mathbf{N}_e\,\mathrm{d}A_k\;. \tag{47}$$

Using Eq. (44) for $\int_0^1 \boldsymbol{T}_k\,\mathrm{d}\alpha$ in Eq. (47), we get the element tangent matrix as

$$\mathbf{L}_{\mathrm{c}}^{e,n+1} \;=\; -\int_{\Gamma^e_{0k}} \mathbf{N}_e^T\,\overline{\overline{\nabla}}\Phi_\ell\,\mathbf{N}_e\,\mathrm{d}A_k\;, \tag{48}$$

where $\overline{\overline{\nabla}}\Phi_\ell$ is given by

$$\overline{\overline{\nabla}}\Phi_\ell \;=\; \frac{\mathcal{S}_1}{\|\Delta\boldsymbol{x}_k\|}\,\Delta\bar{\boldsymbol{x}}_k\otimes\boldsymbol{n}_{\mathrm{p}} \;-\; \frac{2\cdot\mathcal{S}_2}{\|\Delta\boldsymbol{x}_k\|^2}\Delta\bar{\boldsymbol{x}}_k\otimes\Delta\bar{\boldsymbol{x}}_k \;+\; \frac{\mathcal{S}_2}{\|\Delta\boldsymbol{x}_k\|^2}\,\mathbf{I} \;+\; \frac{\partial T_k\left(\boldsymbol{x}_m\right)}{\partial r_s}\,\boldsymbol{n}_{\mathrm{p}}\otimes\boldsymbol{n}_{\mathrm{p}}\;. \tag{49}$$

The scalars $\mathcal{S}_1$ and $\mathcal{S}_2$ are given as

$$\mathcal{S}_1 \;=\; T_k\left(\boldsymbol{x}_k^{n+1}\right) \;-\; \frac{\partial T_k\left(\boldsymbol{x}_m\right)}{\partial r_s}\,\Delta\boldsymbol{x}_k\cdot\boldsymbol{n}_{\mathrm{p}} \;-\; T_k\left(\boldsymbol{x}_m\right)\;, \tag{50}$$

$$\mathcal{S}_2 \;=\; -\Phi_\ell\left(\boldsymbol{x}_k^{n+1}\right) \;+\; \Phi_\ell\left(\boldsymbol{x}_k^{n}\right) + \mathrm{D}\Phi_\ell\left(\boldsymbol{x}_m\right)\cdot\Delta\boldsymbol{x}_k\;. \tag{51}$$

Here, $\boldsymbol{T}_k \;=\; T_k\boldsymbol{n}_{\mathrm{p}}$ where $T_k \;=\; \beta^{\mathrm{s}}_{0k}\,\frac{\partial\Phi_\ell}{\partial r_{\mathrm{s}}}$.

4.3 Schemes used for performance evaluation

As mentioned earlier, so far no temporal discretization scheme has been applied for dynamic adhesive contact problems. However, collocation based schemes can also be used for temporal discretization. In the discussions that follow, the performance of the proposed scheme is also compared with two collocation based schemes. The schemes selected are the Newmark scheme (Newmark, 1959) and a composite scheme recently proposed by Bathe (2007). Newmark's scheme falls in the category of *parameter-based family of collocation schemes* as two parameters, usually denoted by γ and β, are needed in the approximation formulas for displacement and velocities. In the present work, $\gamma \;=\; 1/2$ and $\beta \;=\; \gamma/2$ are chosen which conserves energy and momentum for linear systems. The composite scheme proposed by Bathe (2007) falls in the category of *parameter-free family of collocation schemes* as no parameter is needed to be chosen or adjusted.

5 Numerical Example 1: Analysis of a single degree of freedom adhesion problem

In this section, we investigate the adhesive contact between two mass points, see Fig. (2). The interaction of the moving mass with the fixed mass is assumed to be governed by an interaction potential $\Pi_c = \phi(x)$ where $\phi(x)$ is given by Eq. (9). Two cases are analyzed viz., with both the internal and contact energies ($\Pi = \Pi_{int} + \Pi_c$, see Fig. 2(a)) and with the contact energy ($\Pi = \Pi_c$, see Fig. 2(b)). The total energy, E, of the system shown in Fig. 2(a) is given by

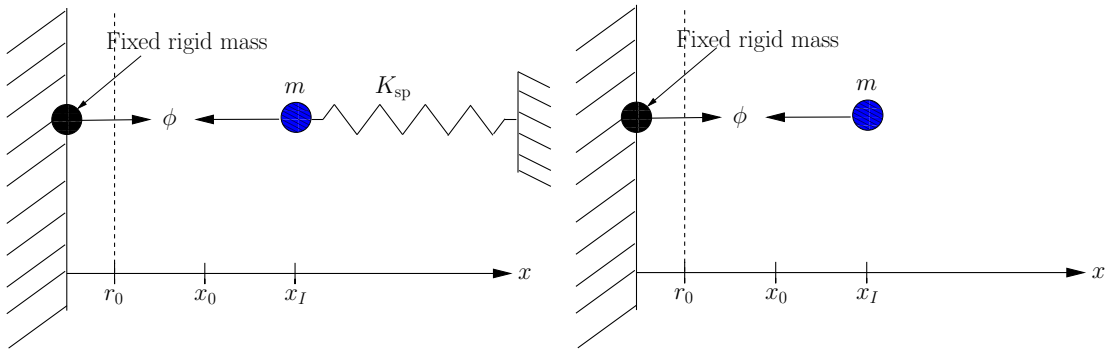

(a) $\Pi = \Pi_{int} + \Pi_c$ (b) $\Pi = \Pi_c$

Figure 2: Two point masses interacting with $\Pi_c = \phi(x)$, see Eq. (9). In (a) the moving mass is assumed to have an internal energy source modeled as a spring while in (b) the moving mass has only contact energy.

$$E = K + \Pi = \frac{1}{2} m \dot{x}^2 + \frac{1}{2} k_{sp} (x - x_0)^2 + \Pi_c \,, \tag{52}$$

where k_{sp} is the spring stiffness and x_0 is the equilibrium position of the spring-mass system alone. The equation of motion is obtained by setting $\partial E / \partial t = 0$ which, $\forall \dot{x}$, leads to

$$m\ddot{x} + \underbrace{k_{sp}(x - x_0)}_{\text{term 1}} + \underbrace{\phi_{,x}}_{\text{term 2}} = 0 \,. \tag{53}$$

To analyze the problem, Eq. (53) is first nondimensionalized. When both terms 1 and 2 are considered (Fig 2(a)), Eq. (53) is nondimensionalized by first defining

$$X = \frac{x}{x_0} \,, \qquad X'' = \frac{1}{\omega^2} \ddot{X}, \qquad \omega = \sqrt{\frac{k_{sp}}{m}} \,, \tag{54}$$

and using the following parameter definitions

$$\gamma_K = \frac{k_{sp}}{k_c} \,, \qquad \gamma_L = \frac{x_0}{r_0} \,, \qquad \gamma_I = \frac{x_I}{x_0} \,. \tag{55}$$

The parameter γ_K characterizes the ratio of the stiffness of the system with respect to the static contact stiffness. The static contact stiffness $k_c = 36 \cdot (4/13)^{4/3} \cdot \left(\epsilon / r_0^2\right)$ is defined as the critical contact stiffness corresponding to static adhesion (Sauer, 2011a). The parameter γ_L characterizes the range of adhesion. As the value of γ_L increases the range of interaction of the moving mass with the fixed mass decreases. The parameter γ_I characterizes the ratio of initial position of the moving mass with the equilibrium position of the spring-mass system alone. With the preceding definitions, the nondimensionalized equation is written as

$$X'' + (X - 1) - \frac{\alpha_0 \gamma_K^{-1}}{\gamma_L^8} \left(\gamma_L^{-6} X^{-13} - X^{-7} \right) = 0 \,, \tag{56}$$

where $\alpha_0 = (1/3) \cdot (13/4)^{4/3}$. However, when the internal energy is not considered (Fig 2(b)) i.e., term 1 is dropped in Eq. (53), the nondimensionalized equation is obtained by defining

$$X'' = \frac{1}{\omega^2}\ddot{X}, \qquad \omega = \sqrt{\frac{k_c}{m}} \, . \tag{57}$$

The definitions for γ_L and γ_I remain unchanged. The nondimensionalized equation is then given by

$$X'' - \frac{\alpha_0}{\gamma_L^8}\left(\gamma_L^{-6} X^{-13} - X^{-7}\right) = 0 \, . \tag{58}$$

5.1 Numerical Analysis

In this section, the numerical behavior of the problem shown in Fig (2) is investigated using the proposed temporal discretization scheme, see section 4 and based on Eq. (44). In the discussions that follow this scheme is referred to as Proposed DG scheme. First, the performance of the proposed temporal discretization scheme discussed in section 4 is compared with other schemes. Then, the effect of the parameters γ_I, γ_K, and γ_L on the solution is investigated. A study to determine the time step required to attain a specified error in energy for a range of values of γ_I, γ_K, and γ_L is carried out in the end.

5.1.1 Performance of various schemes.

First, the performance of various temporal discretization schemes is assessed for the two cases shown in Fig. 2. The result for the case when Gauss quadrature rule is used to perform integration of Eqs. (33) and (34) is also included. It is referred as Proposed SQ scheme in further text. For each case the value of γ_I, γ_L, and γ_K are chosen as 3, 1, and 1 respectively. This case corresponds to impact dominated problem, see section 2.2 and appendix A for details. For each scheme, the logarithm of relative error in the computed energy, E_{err}, is studied. It is defined as

$$E_{\text{err}} := \log_{10}\left[\frac{E_0 - E_n}{E_0}\right] \, , \tag{59}$$

where E_0 and E_n are the energies at the start and at time $t = t_n$ respectively.

Figure (3) shows the variation of E_{err} with time for the different schemes. It is seen that the composite scheme exhibits large error. Newmark's scheme shows higher error during impact phase but regains some of its accuracy once the impact is over. The energy-momentum conserving schemes i.e., Proposed DG and Proposed SQ schemes, exhibit very small error. Table (1) shows the maximum error obtained for 2 impacts using various schemes. The error corresponding to a third case where only internal energy i.e., $\Pi = \Pi_{\text{int}}$ is considered, is also included. It can be seen that incorporation of contact greatly reduces the accuracy of collocation based schemes i.e., Newmark, Bathe schemes while it has very little influence on the accuracy of momentum based schemes.

5.1.2 Effect of γ_I, γ_K, and γ_L.

First, the effect of the parameters used in the nondimensionalization of Eq. (53) on the solution is studied using the Proposed DG and Newmark scheme. Both the internal and contact energies are considered (Fig. 2(a)). We refer to the appendix A for a discussion on the selection of values for γ_I, γ_K, and γ_L. Five different values each for γ_I, γ_K, and γ_L are chosen for the

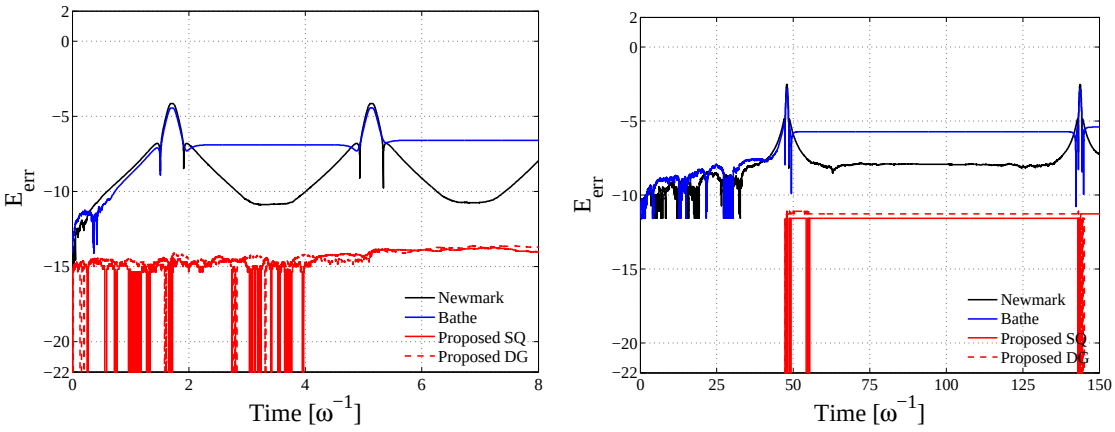

(a) $\Pi = \Pi_{\text{int}} + \Pi_{\text{c}}$ (b) $\Pi = \Pi_{\text{c}}$

Figure 3: Variation of error E_{err} over time for all the schemes. Figure (a) is obtained using the linearized Eq. (56) while Fig. (b) is obtained using the linearized Eq. (58).

Table 1: Maximum error in energy obtained using different schemes.

Temporal scheme	E_{err} ($\Pi = \Pi_{\text{int}} + \Pi_{\text{c}}$)	E_{err} ($\Pi = \Pi_{\text{c}}$)	E_{err} ($\Pi = \Pi_{\text{int}}$)
Newmark (Newmark, 1959)	-4.14	-2.53	-10.57
Bathe (Bathe, 2007)	-4.44	-2.83	-10.00
Proposed SQ	-13.72	-11.09	-13.94
Proposed DG	-13.62	-11.09	-14.02

simulation. They are: $\gamma_I = [0.50, 0.90, 1.40, 3.00, 10.00]$, $\gamma_K = [0.50, 0.75, 1.00, 3.00, 10.00]$, and $\gamma_L = [1.00, 1.10, 1.20, 1.30, 1.40]$ respectively.

Figure (4) shows the maximum E_{err} for the Newmark and Proposed DG schemes for three different values of γ_I. In all cases, the error for Newmark's scheme is higher than for the Proposed DG scheme. It is observed that the maximum error in not much affected by either γ_L or γ_K for both the schemes for $\gamma_I = 0.90$ and $\gamma_I = 1.40$. Also, the maximum E_{err} lies in between -3.00 and -14.00 for both the schemes. The plot of the maximum E_{err} for $\gamma_I = 0.50$ is shown in Fig. (4(c)). It can be seen that as the value of γ_L or γ_K goes down, the maximum error of both the schemes increases. The increase in the error is more for the Proposed DG scheme.

Next, we study the effect of γ_I, γ_K, and γ_L on the time step required to attain a specified error in the total energy. The Proposed DG scheme is used for temporal discretization. Figure (5) shows the log plot of the maximum time step required to attain an error of $E_{\text{err}} \leq -6.00$ for $\gamma_I = 0.90$ and $\gamma_I = 1.40$. The criterion proposed in section 2.2 is used to identify each case as either impact dominated, adhesion dominated or neither. The points have been marked accordingly on the surface. It can be seen that some values correspond to adhesion energy dominated cases ($\bullet$) while some are impact energy dominated cases ($\circ$). The cases where the internal energy dominates the solution are left unmarked. The case for $\gamma_I = 0.50$ is not shown as all the cases are impact dominated. It can be seen that for $\gamma_I = 0.90$ as the value of γ_K increases the time step required to attain a specified error increases. However, for $\gamma_I = 1.40$

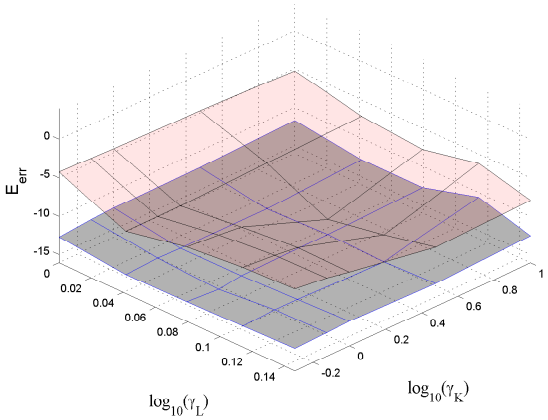

(a) $\gamma_I = 0.90$

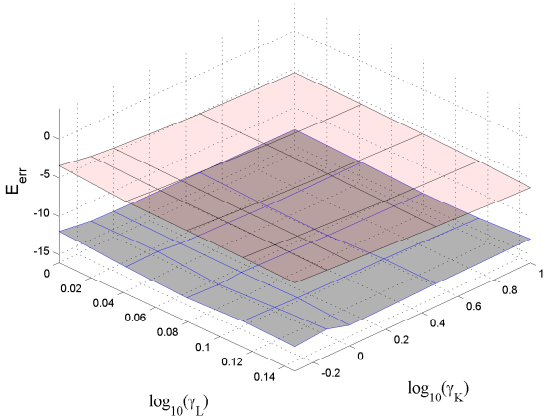

(b) $\gamma_I = 1.40$

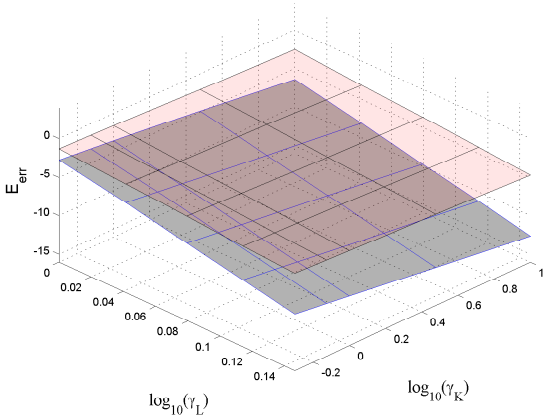

(c) $\gamma_I = 0.50$

Figure 4: Plot of maximum E_{err} for $\Delta t = 0.001$ $[\omega^{-1}]$ for the case $\Pi = \Pi_{\text{int}} + \Pi_{\text{c}}$. The parameters γ_I, γ_K, and γ_L correspond to the initial position of moving mass, adhesion strength, and length scale respectively. The light color surface is for Newmark scheme and the dark color surface is for Proposed DG scheme.

there is very little effect of γ_L or γ_K on the required time step. Hence, the proposed scheme is equally good for all the values of γ_L and γ_K.

5.2 Physical Analysis

In this section, several physical properties of the problem shown in Fig (2) are discussed. The Proposed DG scheme is used for all numerical simulations. The value of γ_I, γ_L, and γ_K are chosen as 3, 1, and 1 respectively. First, the variation of different energies over time is studied. Then the principal equivalence of the two interaction potentials discussed in section 2.1 (i.e., Eqs. 8 and 10) is shown.

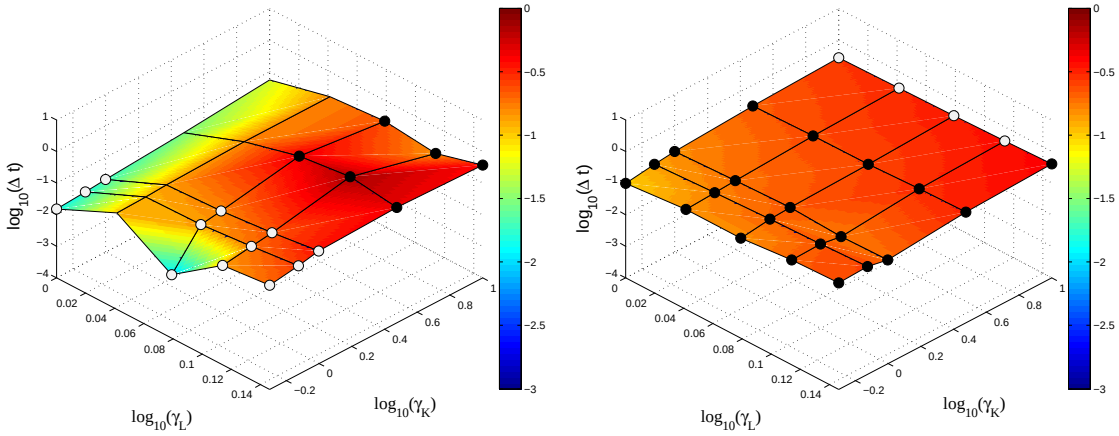

(a) $\gamma_I = 0.90$ (b) $\gamma_I = 1.40$

Figure 5: Log plot of maximum time step Δt required for achieving $E_{\text{err}} \leq -6.00$ ($\Pi = \Pi_{\text{int}} + \Pi_{\text{c}}$). The black points ($\bullet$) denote the adhesion energy dominated cases while the white points ($\circ$) denote the impact energy dominated cases. The cases which are dominated by internal energy are left unmarked.

5.2.1 Phase space plot.

First, the phase space plots for both the cases (Fig. 2) are shown in Fig (6). It can be observed that when only the contact energy is considered ($\Pi = \Pi_{\text{c}}$), the phase space plot differs remarkably from that when only internal energy is considered ($\Pi = \Pi_{\text{int}}$). However, when both the internal and the contact energies are considered ($\Pi = \Pi_{\text{int}} + \Pi_{\text{c}}$), the effect of adhesion is felt only near the equilibrium position. The effect of adhesion is marked with arrows. When the moving mass passes to the repulsion zone i.e., impact phase, the proposed augmentation to the Proposed DG scheme is able to capture the highly nonlinear behavior very accurately for both the cases.

5.2.2 Variation of different energies over time.

The variation of the energy fractions (normalized by maximum kinetic energy) over time is shown in Figs. (7) and (8) for the two cases shown in Fig. 2. It is observed that for the first case (Fig. 7), the fraction of adhesion energy Π_{adh} (as discussed in section 2.2) is very small compared to the kinetic, potential, or impact energy Π_{rep} for most of the period. For clarity, the zoomed view of Fig. (7(a)) is shown in Fig. (7(b)) for one particular cycle of interaction. Hence, this case is classified as an impact dominated problem (see section 2.2 for discussion). However, when only the contact energy is considered (i.e., $\Pi = \Pi_{\text{c}}$) the fraction of adhesion energy Π_{adh} is equally large when compared to other energies i.e., the kinetic, and the impact energy Π_{rep}, see Figs. (8) and (8(b)). Hence, this case is equally dominated by both adhesion and impact.

5.2.3 Comparison of two different interaction models.

In this section, the two interaction models mentioned in section 2.1 are applied to second case (i.e, $\Pi = \Pi_{\text{c}}$, see Fig. 2(b)). The aim is to show that the current analysis and its conclusions are general and apply equivalently to the two kind of potentials introduced. Therefore, the

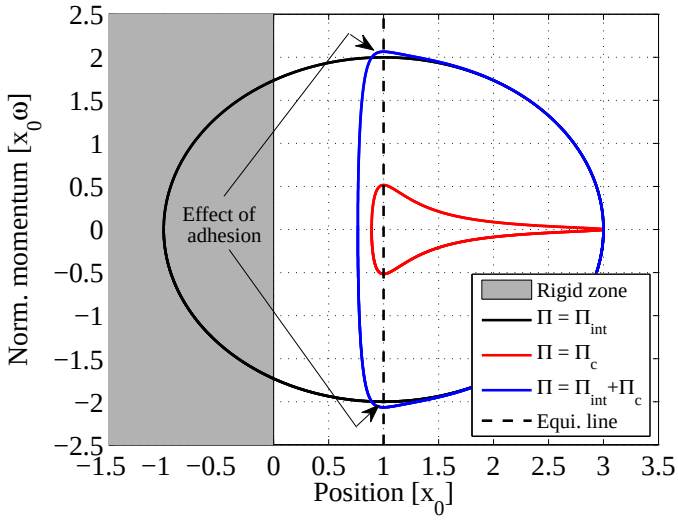

Figure 6: Phase space plot. The effect of adhesion on the system is marked with arrows. It can be seen that adhesion is important only when the moving mass is near to the equilibrium line. When $\Pi = \Pi_c$, the moving mass takes a long time to approach the equilibrium line due to the weak attraction at great distance.

exponential cohesive zone (CZ) model is scaled and shifted so as to match as closely as possible to the Lennard-Jones (LJ) potential (Eq. 9). The criterion used are: (a) the shape of traction curve, (b) position of equilibrium point, and (c) the critical stiffness of the potentials. Then, following identical procedure, the nondimensionalized equation for the exponential cohesive zone model (Eq. 10) is written as

$$X'' + X\,\gamma_L \exp\left(-X\gamma_L\right) = 0\ , \tag{60}$$

where X and γ_L have been defined in Eqs. (54) and (55) respectively. The value of γ_I and γ_L are chosen as 3 and 8.33 respectively. The force-gap plots for the two models are shown in Fig. (9(a)). The corresponding phase space plot for the two models is shown in Fig. (9(b)). It can be seen that the two responses are similar. However, the CZ model has lower velocity than the LJ model for the same position. This is since is the CZ model goes asymptotically to zero faster than LJ model. Hence, the moving mass experiences smaller attraction force for CZ model for large distance and accelerates slowly. However, the overall nature of the response obtained using the two models is similar which establishes the general nature of the formulation.

5.2.4 Effect of strong and weak adhesion.

Finally, the effect of strong and weak adhesion is studied using the CZ model. We now also consider the case with $\gamma_L = 1$. The force gap plot for the CZ model for the two set of parameter values is shown in Fig (10(a)). It should be noted that the equilibrium position and the value of maximum adhesive force remain same. However, now the adhesion energy has been increased significantly and the repulsion energy has decreased. The phase space plot is shown in Fig. (10(b)). It can be seen that the moving mass has higher velocity for the same position for strong adhesion. This is since the adhesion energy is now much more than the case with weak adhesion. However, in the repulsion phase, the mass point moves much closer to the fixed mass point for the case with strong adhesion as the repulsion energy is much lower.

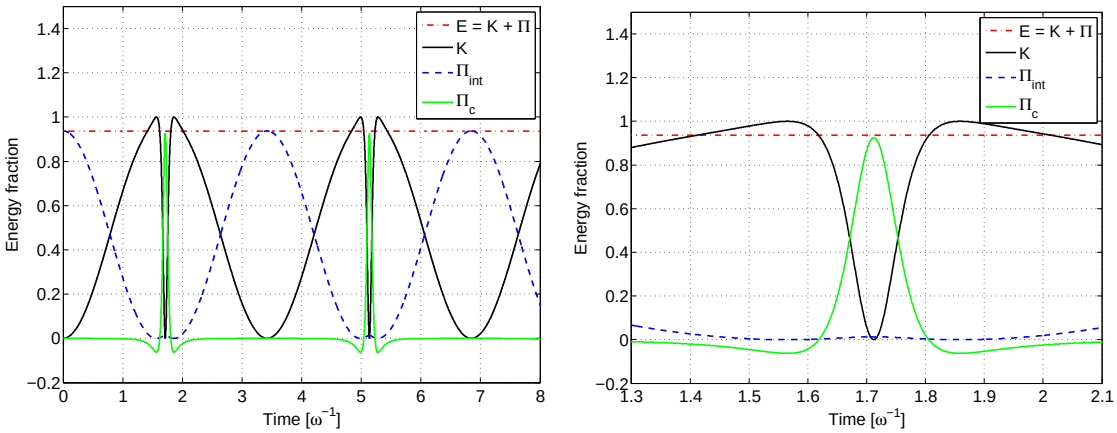

(a) Energy fraction (b) Energy fraction (zoomed view)

Figure 7: Variation of the different energy fractions over time using the Proposed DG scheme considering $\Pi = \Pi_{\text{int}} + \Pi_{\text{c}}$. The plot is normalized by maximum kinetic energy and ω of Eq. (54).

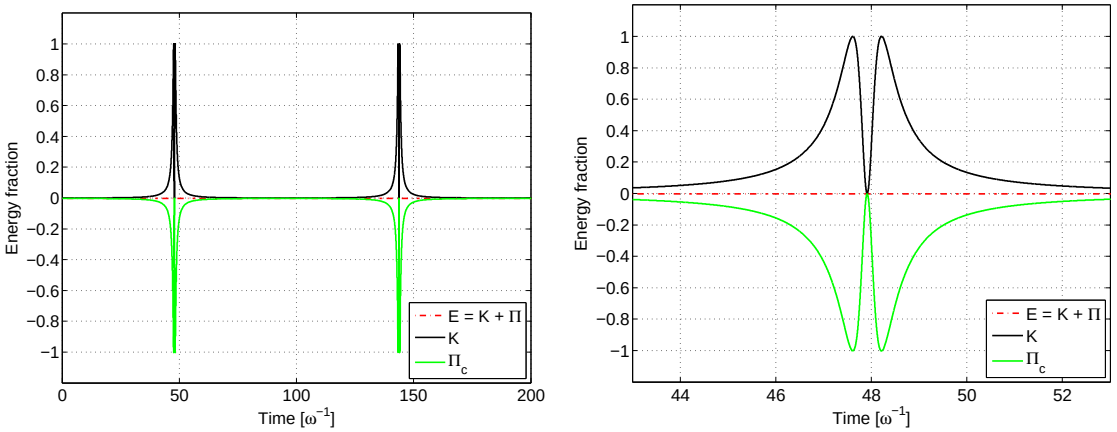

(a) Energy fraction (b) Energy fraction (zoomed view)

Figure 8: Variation of the different energy fractions over time using the Proposed DG scheme considering $\Pi = \Pi_{\text{c}}$. The plot is normalized by maximum kinetic energy and ω of Eq. (57).

6 Numerical Example 2: Analysis of multi degree of freedom adhesion problem

In this section, analysis of a multi degree of freedom adhesion problem is considered, see Figure (11). The diameter of the ball is $D = 10\ L_0$ ($L_0 = 1$ nm) and the initial separation is taken as $h_0 = 2\ L_0$. The material parameters μ and Λ are taken as 0.8333 GPa and 0.5556 GPa ($E = 2$ GPa and $\nu = 0.2$) respectively. The density of the ball is taken as 1000 kg/m^3. The ball is initially at rest and the interaction is assumed to be governed by the interaction potential Φ_ℓ given in Eq. (8). The traction is then given by Eq. (7). In the present work a normalized form of Eq. (7) is used. For normalization of Eq. (7), we first define

$$\bar{\boldsymbol{T}}_k = \frac{\boldsymbol{T}_k}{E_0}\ , \qquad \bar{r}_{\text{s}} = \frac{L_0}{r_{\text{s}}}\ , \tag{61}$$

where E_0 and L_0 are the characteristic energy density (or stiffness) and length scale of the problem respectively. The normalized equation corresponding to Eq. (7) is written using the

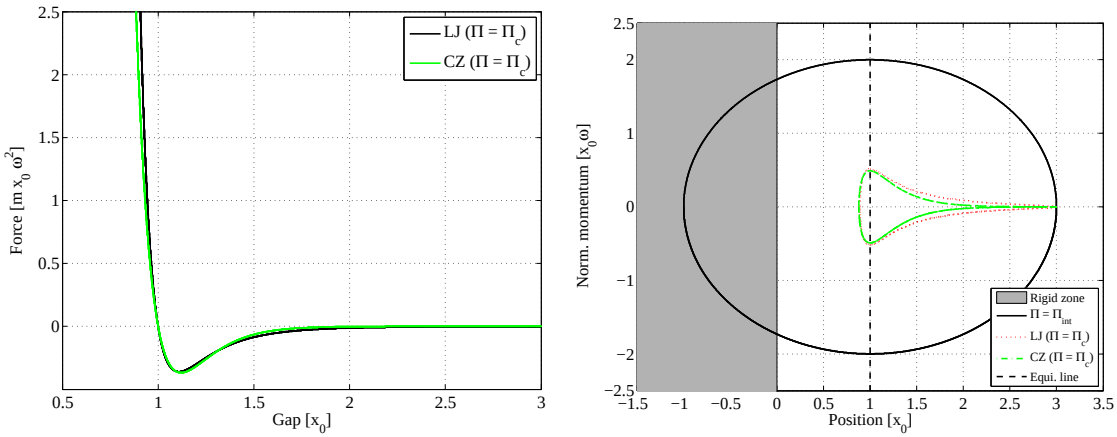

(a) Force with gap (b) Phase portrait

Figure 9: Comparison of LJ potential given by Eq. (9) with $\gamma_L = 1$ and exponential CZ model given by Eq. (10) with $\gamma_L = 8.33$ when only the contact energy is considered i.e., $\Pi = \Pi_c$.

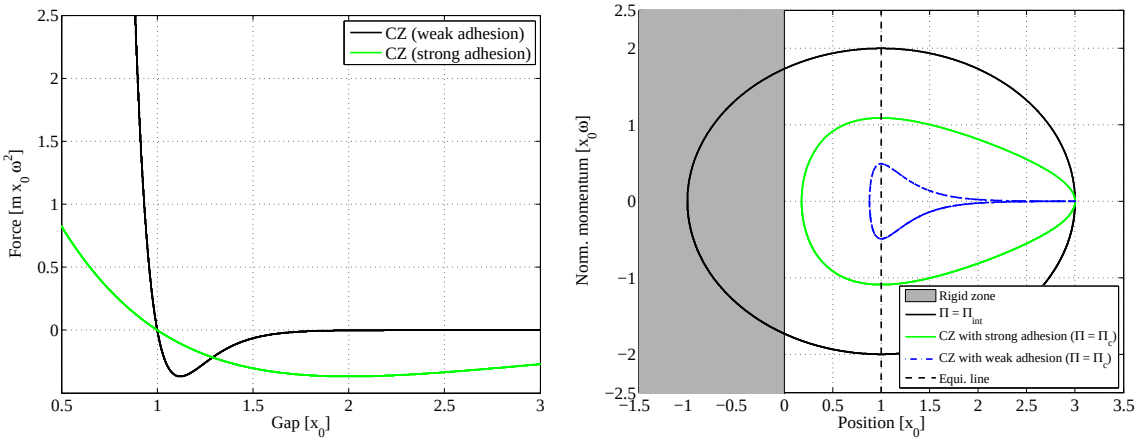

(a) Force with gap (b) Phase portrait

Figure 10: Effect of adhesion using the exponential CZ model given by Eq. (10) when only the contact energy is considered i.e., $\Pi = \Pi_c$. For strong adhesion: $\gamma_L = 1$ and for weak adhesion: $\gamma_L = 8.33$.

normalization procedure discussed in Sauer and Li (2007), which leads to

$$\bar{\boldsymbol{T}}_k = \left[\frac{c_1}{\bar{r}_s^9} - \frac{c_2}{\bar{r}_s^3}\right] \boldsymbol{n}_p = \bar{T}_k \boldsymbol{n}_p \ , \tag{62}$$

where the constants c_1 and c_2 are given as

$$c_1 = \frac{\pi}{45\gamma_W \gamma_L^9}, \qquad c_2 = \frac{\pi}{3\gamma_W \gamma_L^3}. \tag{63}$$

The parameters $\gamma_L = L_0/r_0$ and $\gamma_W = E_0/w_0$, where $w_0 = A_H/2\pi^2 r_0^3$, characterize the scale and strength of adhesion. We refer to Sauer and Li (2007) for detailed discussion on γ_L and γ_W. Two different cases are considered: (i) $\gamma_L = 2.5$, $\gamma_W = 25$, and (ii) $\gamma_L = 1$, $\gamma_W = 100$. Case 1 corresponds to parameters of gecko adhesion (Sauer, 2009) while case 2 corresponds to very small adhesion energy. The time step for the analysis is taken as 0.001 T_0 ($T_0 = 1$ ns). Three different initial mesh configurations for the ball are considered, see Table 2.

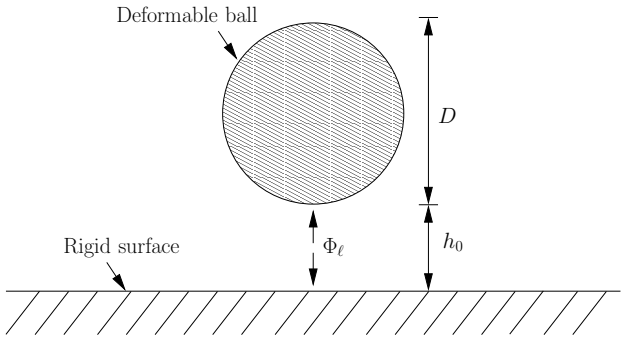

Figure 11: Initial configuration for study of interaction of a soft ball with a rigid surface. The interaction is governed by the interaction potential Φ_ℓ according to Eq. (8). The diameter of the ball is taken as $D = 10L_0$ and the initial separation is taken as $h_0 = 2L_0 + r_{\text{eq}}$ where $L_0 = 1\text{nm}$ and r_{eq} is the equilibrium distance corresponding to the interaction potential Φ_ℓ. The ball is assumed to be at rest at $t = 0$.

Table 2: Finite element mesh details for soft ball impact with a rigid surface.

Mesh No.	No. of elements	No. of dofs
1	48	114
2	192	418
3	768	1602

Before we present the results, it is mentioned again that "Proposed DG scheme" denotes the temporal discretization scheme based on discrete gradient, see section 4 and Eq. (44). The phrase "Proposed SQ scheme" is when standard Gaussian quadrature rule is used for evaluating the integrals in Eqs. (33) and (34). The initial and deformed configuration of the system is shown in Fig. (12) for the finest mesh i.e., mesh 3. The contour of the first invariant of the stress is also shown. Figure (12(b)) shows the deformed configuration at time $t = 0.28\,T_0$. The adhesion zone is marked. In this zone, the material particles are attracted towards the rigid surface. The zone of negative stresses is called the impact zone. In this zone the material particles are repelled from the rigid surface. A sharp transition from impact zone to adhesion zone can also be seen. For more discussion on the characteristics of these zones we refer to references Sauer and Li (2007); Sauer and Wriggers (2009).

6.1 Conservation of the total energy and total angular momentum

The performance of various temporal integration schemes is investigated. Figure (13) shows the variation of E_{err} (see Eq. 59) over time for case 1 and case 2 using various temporal discretization schemes discussed in section 4. Mesh 1 is used for the analysis. It is observed that the Newmark scheme diverges after some time for case 1. The composite scheme exhibits large error. It should be noted that for case 2 (Fig. 13(b)), the Proposed DG scheme does not exhibit any error within the machine precision. However, for case 1 (Fig. 13(a)), the Proposed DG scheme exhibits some error in the energy but still has the lowest error among all the schemes. Also, it should be noticed that the accuracy of each scheme, particularly for case 1, is now much lower when compared to the problem considered in section 5. This is because the ball is considered as a continuum rather than a single degree of freedom system. Hence, dynamic effects like stress wave propagation and higher mode excitation now affect the solution. Figures (13(c)) and (13(d)) show the variation of logarithmic norm of total angular momentum with time for different schemes. It should be

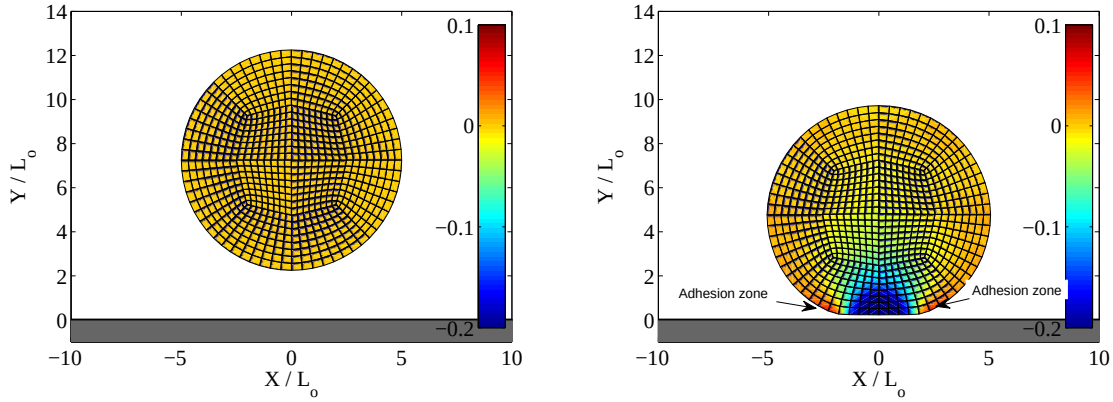

(a) $t = 0.00\,T_0$ (b) $t = 0.28\,T_0$

Figure 12: Deformed configuration of the ball for the Proposed DG scheme using mesh 3 and $\Delta t = 0.001\,T_0$ (case 1: $\gamma_L = 2.5$, $\gamma_W = 25$). The adhesion zone has been marked with arrow. The first invariant of the stress is shown. The stress values are normalized by E_0. A sharp transition from impact zone i.e., where stress is negative, to adhesion zone i.e., where stress is positive, can also be seen.

noted that the ball is initially at rest so that the norm of total angular momentum, $\|\mathbf{G}_{n+1}\|$, is zero. The wild fluctuations of the total angular momentum in all cases is due to the non-linear contact potential. Now for weak adhesion, all schemes show similar result. However, for the case of strong adhesion the Proposed DG scheme shows higher error. It is pointed out that for finer meshes, i.e. Mesh 2 and Mesh 3, the Proposed DG scheme performs slightly better than the other schemes.

Next, the Proposed DG scheme is used to analyze the problem for different time steps and mesh discretizations. The interaction parameters are taken as $\gamma_L = 2.5$, $\gamma_W = 25$. The objective is to study the effect of time step size and mesh discretization. Figure (14(a)) shows the plot of E_{err} with time for three different time steps. It is seen that for time step $\Delta t = 0.0001\,T_0$ the error is minimum while it is maximum for $\Delta t = 0.001\,T_0$. This may be because as the time step is lowered, spurious higher modes are excited. Another source of this behavior is because the value of $\|\Delta \boldsymbol{x}_k\|$ in Eq. (44) approaches a very small value. Division by these small values will also lead to loss in accuracy. Some discussion on the numerical limit behavior of the term $\|\Delta \boldsymbol{x}_k\|$ has been discussed in Mohr et al. (2008). Figure (14(b)) shows the error for three different finite element mesh discretizations. It is observed that E_{err} goes down with mesh refinement. Figures (14(c)) and (14(d)) show the variation of logarithmic norm of angular momentum with time for different time steps and mesh. Lowering of the time step results in a behavior similar to that observed in Fig. (14(a)). As in case of energy error, refining the mesh leads to better accuracy as observed in Fig. (14(d)).

6.2 Variation of contact force and contact gap

In this section, the variation of the total contact force and the distance between the bottom node from the rigid surface is investigated for different time steps and mesh discretizations. The total contact force is given as the sum of all the finite element forces on the contact surface. It is defined as

$$\mathbf{P}_{\text{c}} := \sum_{N=1}^{n_n} \mathbf{f}_{\text{c}}^N. \tag{64}$$

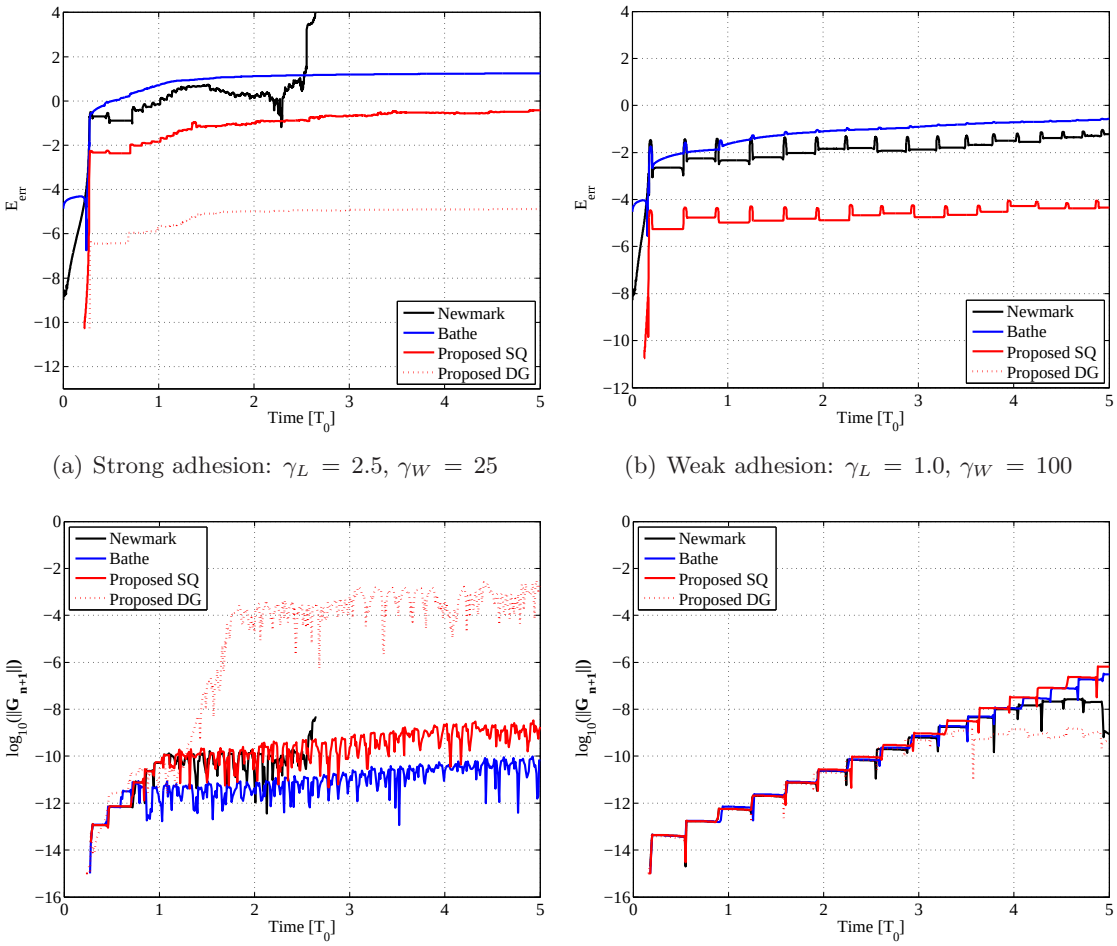

(a) Strong adhesion: $\gamma_L = 2.5$, $\gamma_W = 25$

(b) Weak adhesion: $\gamma_L = 1.0$, $\gamma_W = 100$

(c) Strong adhesion: $\gamma_L = 2.5$, $\gamma_W = 25$

(d) Weak adhesion: $\gamma_L = 1.0$, $\gamma_W = 100$

Figure 13: Variation of error E_{err} and $\log_{10}(\|\mathbf{G}_{n+1}\|)$ over time for various schemes (using mesh 1 and $\Delta t = 0.001\,T_0$). In (a), it can be seen that the Newmark scheme diverges after some time. In (b), the Proposed DG scheme shows an error on the order of machine precision. Hence, it is absent from the plot.

The distance between the bottom node of the ball from the rigid surface at time t is defined as

$$h(t) := r_s(t) + r_{\text{eq}} \,, \tag{65}$$

where $r_s(t)$ is the contact gap and r_{eq} is the equilibrium distance corresponding to the interaction potential Φ_ℓ.

First, the variation of vertical component of $\mathbf{P}_{\text{c}}$ over time is analyzed, see Fig. (15). Impact occurs when the contact force changes from adhesion to repulsion (i.e., when the value changes sign). The impact ends when the contact force changes from repulsion to adhesion (i.e., when the value goes from negative to positive). Different material points will undergo impact at different instances in time. Hence, Fig. (15) shows an overall behavior. First, the effect of the time step is analyzed. Figure (15(a)) shows the plot of the total contact force with time for different time steps. It is seen that for all the time steps, the response is similar up to $t < 0.40\,T_0$. It is also observed that as the time step goes down, more fine scale oscillations are observed in the response, see Fig. (16). Again, this is because as the time step is lowered, first, higher modes get excited. Secondly, the numerical limit behavior for very small values of term $\|\Delta \boldsymbol{x}_k\|$ (see Eq. (44)) also leads to a loss in accuracy. This shows that after the first 2 impacts, the solution

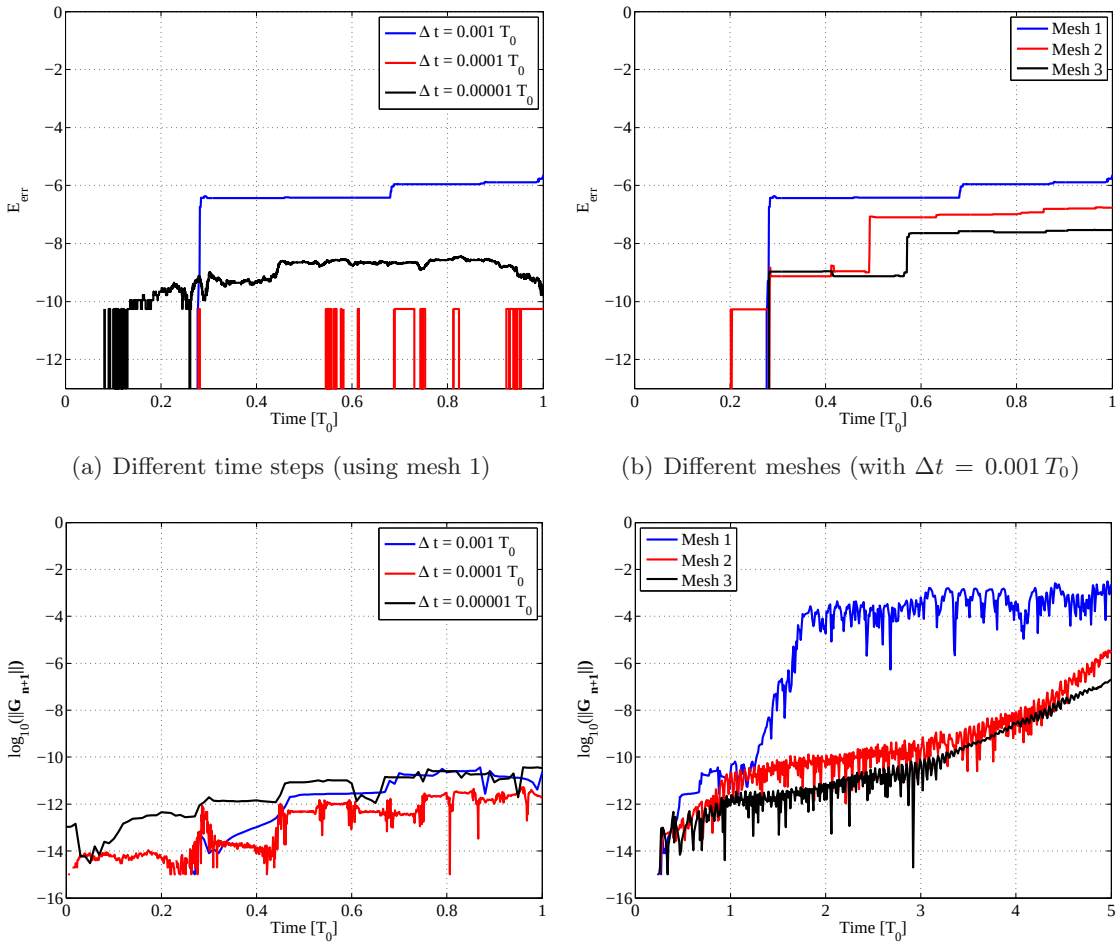

(a) Different time steps (using mesh 1)

(b) Different meshes (with $\Delta t = 0.001\,T_0$)

(c) Different time steps (using mesh 1)

(d) Different meshes (with $\Delta t = 0.001\,T_0$)

Figure 14: Variation of error E_{err} and $\log_{10}(\|\mathbf{G}_{n+1}\|)$ over time ($\gamma_L = 2.5$, $\gamma_W = 25$) for the Proposed DG scheme. It should be noted that when the error is less than machine precision, it is not shown. The vertical lines in (a) and (b) show the jump in error from machine precision values to higher values.

of the problem no longer represents the actual behavior. Hence, no specific conclusions should drawn beyond a certain time. However, it does show the long time stability characteristic of the proposed scheme. One possible remedy to alleviate this behavior is to incorporate some form of damping into the system. Another possible remedy to address this kind of numerical limit behavior has been discussed by Mohr et al. (2008). Yet another remedy can be to use schemes which dissipate energy of the higher modes. This will, of course, lead to overall loss in energy of system. Figure (15(b)) shows the plot of the total contact force with time for the three different finite element mesh discretizations. It is seen that up to $t < 0.25\,T_0$, the response is similar. However, for $t > 0.25\,T_0$, the response for each mesh is different. Again beyond the first impact no specific conclusion, other than the stability of the proposed scheme, should be drawn.

Figure (17(a)) shows the plot of h over time for different time steps. It is seen that as the time step is reduced, the number of impacts of the ball with the rigid surface also increases. The response for $\Delta t = 0.0001\,T_0$ and $\Delta t = 0.00001\,T_0$ are quite close up to $t < 0.60\,T_0$. Also, it is observed that for smaller time steps the oscillation decreases more rapidly. Figure (17(b)) shows the plot of h over time for the three different mesh discretizations. The response for finer meshes is only similar up to $t < 0.40\,T_0$. Again, beyond the first 2 impacts the solution for

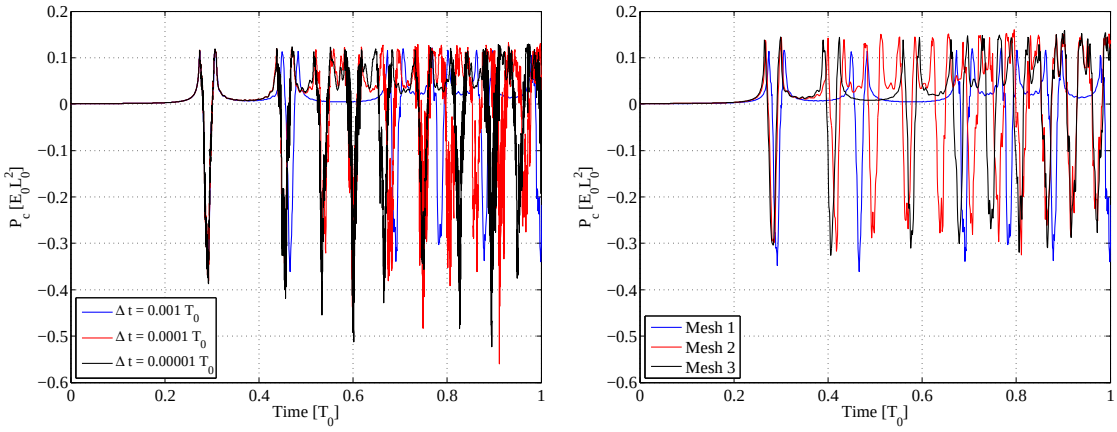

(a) Different time steps (mesh 1)

(b) Different meshes ($\Delta t = 0.001\,T_0$)

Figure 15: Variation of vertical component of $\mathbf{P}_c$ over time for the Proposed DG scheme ($\gamma_L = 2.5$, $\gamma_W = 25$ and using mesh 1). Positive contact force shows adhesion while negative value shows repulsion.

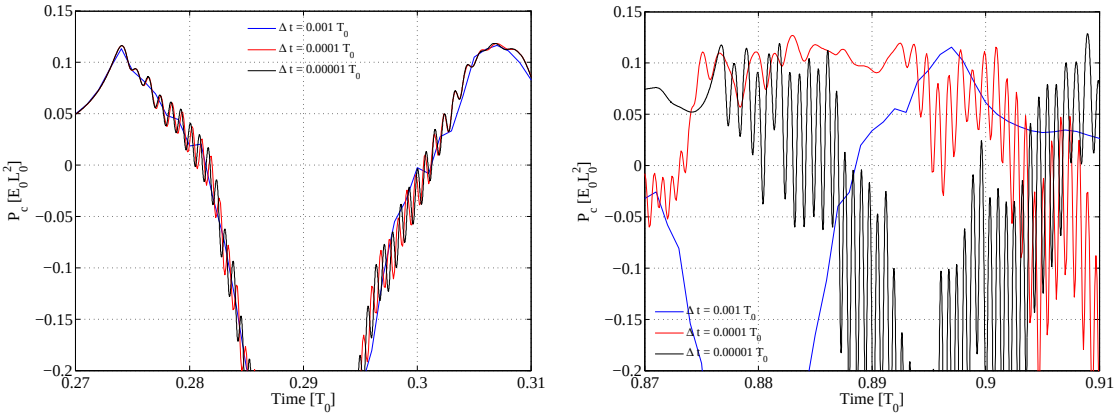

(a) Time period $t \in (0.27\,T_0,\, 0.31\,T_0)$

(b) Time period $t \in (0.87\,T_0,\, 0.91\,T_0)$

Figure 16: Zoomed plot of the variation of vertical component of $\mathbf{P}_c$ over time for the Proposed DG scheme at two different time range ($\gamma_L = 2.5$, $\gamma_W = 25$ and using mesh 1). Fine scale oscillations appear for decreasing Δt.

each case differs from each other appreciably. With these preceding studies, it is observed that the algorithmic energy conservation alone does not ensure correct results of the contact force and the distance, (see Ortiz, 1986).

6.3 Application of enriched contact finite elements

Here, we present a study on using enriched contact finite elements proposed recently, (see Sauer, 2011b). Figure 18 shows the performance of the proposed scheme for various contact finite element formulations. The mesh used is Mesh 2 with $\Delta t = 0.001\,T_0$ and the adhesion parameters are set to $\gamma_L = 2.5$, $\gamma_W = 25$. In the figure, Q1C1 is the bilinear quadrilateral element with linear interpolation of the displacement field at the contact interface. Secondly, Q1C2 is the quadrilateral element enriched with one node on the contact surface leading to quadratic interpolation of the displacement field. Thirdly, Q1C4 is the quadrilateral element enriched with three nodes on the contact surface leading to fourth order approximation of

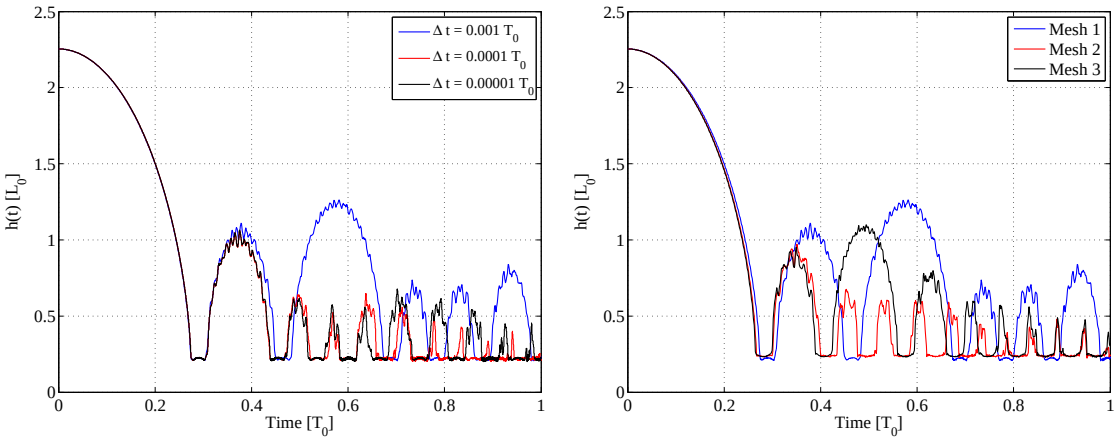

(a) Different time steps (using mesh 1)

(b) Different meshes ($\Delta t = 0.001\,T_0$)

Figure 17: Plot of height $h(t)$ over time for the Proposed DG scheme ($\gamma_L = 2.5$, $\gamma_W = 25$).

the displacement field on the contact interface. Finally, Q1CH is the quadrilateral element where on the contact interface, apart from the nodal displacements, their derivative is also interpolated. Figure 18(a) shows the variation of error E_{err} over time. It is also pointed out, without elaborating further, that for the Newmark scheme, the divergence behavior observed in Fig. (13(a)) is not observed when using the enriched contact elements. It can be seen that the error in the energy goes down when enriched contact finite elements are incorporated. However, no specific trend is observed for the different enriched contact elements. The reason for the improved performance, when using the enriched elements, is that the contact forces are captured more accurately. Figure 18(b) shows the plot of h over time for the various contact finite element formulations. It is seen that the response of the different enriched elements is similar for the first two impacts after which they start to differ. As discussed earlier, beyond the second impact no specific conclusions should be drawn.

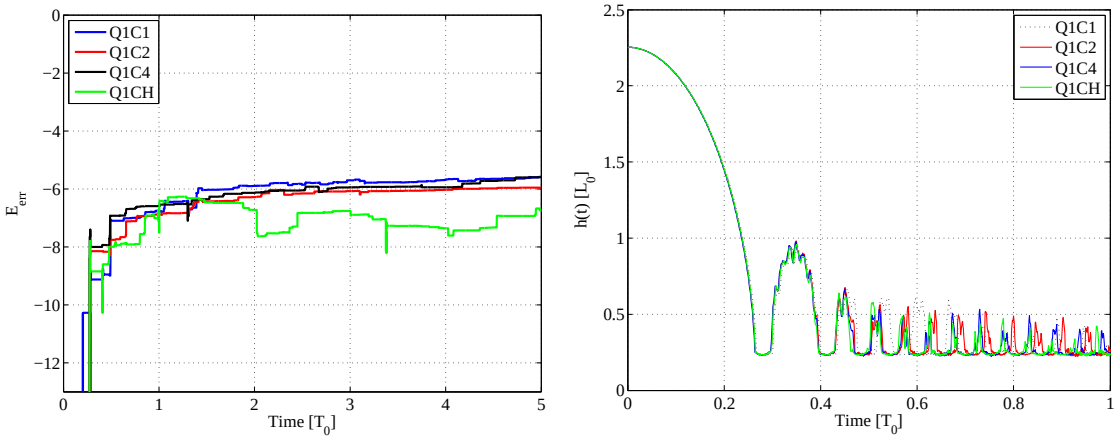

(a) E_{err} over time

(b) Height $h(t)$ over time

Figure 18: Variation of error E_{err} and height $h(t)$ over time for the Proposed DG scheme with various contact finite elements using mesh 2 ($\Delta t = 0.001\,T_0$ and $\gamma_L = 2.5$, $\gamma_W = 25$).

7 Conclusions

In the present work, a new energy-momentum-conserving temporal discretization scheme is proposed for the computation of adhesive contact problems. A contact criterion is also proposed to distinguish between adhesion-dominated and impact-dominated contact behavior. The proposed scheme adds very little to the computational cost. The performance of the proposed scheme is compared with both parameter-based and parameter-free families of collocation based schemes for single degree and multi degree of freedom systems. It is found that the proposed schemes shows major accuracy gains in conserving energy. However, it is found that reducing the time step or mesh leads to different solution beyond the first few impacts. Hence, energy conservation alone does not ensure correct and convergent results. Finally, it is shown that the use of enriched contact finite elements leads to improved behavior without the need to refine the bulk of the domain. However, beyond the first few impacts the solutions differ for each case. The presented work is highly relevant to general adhesion and debonding problems which will be studied in the future. Further considerations are incorporation of the frictional contact. To damp the unwanted physical modes an appropriate form of damping, numerical or physical, will also be studied in the future.

Appendix A: Discussion on selection of values for γ_I, γ_K and γ_L

In this appendix, we present the fact that at least for energy-conserving single particle systems, it is possible to know a priori whether the problem will be an adhesion dominated problem, impact dominated problem or internal energy dominated problem. For single particles, the total energy (i.e., the Hamiltonian) at time $t = 0$ can be written as (assuming the distance of the particle from the wall at $t = 0$ is such that $r_{\text{adh}} > r_{\text{eq}}$)

$$E_0 = \Pi_{\text{int}}\left(t = 0\right) + \Pi_{\text{c}}^{\text{adh}} \ . \tag{A.1}$$

Note that at time $t = 0$ it is assumed that there is no kinetic energy. Now, the total energy at time $t = t^*$, where t^* is the time at which $r_s = r_{\text{rep}}$, is given by

$$E_{t^*} = \Pi_{\text{int}}\left(t = t^*\right) + \Pi_{\text{c}}^{\text{rep}} \ . \tag{A.2}$$

Again, it is pointed out that at $t = t^*$, the kinetic energy is 0. Now, balancing total energy at time $t = 0$ and at time $t = t^*$, we get

$$\Pi_{\text{int}}\left(t = t^*\right) + \Pi_{\text{c}}^{\text{rep}} = \Pi_{\text{int}}\left(t = 0\right) + \Pi_{\text{c}}^{\text{adh}} \ . \tag{A.3}$$

It should be noted that the values at $t = 0$ are known, whereas the quantities at $t = t^*$ depend on $r_s = r_{\text{rep}}$ at $t = t^*$. Now, the above equation is a nonlinear equation in r_{rep} which can be solved using an iterative scheme. Now, we define

$$\Pi_{\text{int}}^{\text{max}} = \max\left(\Pi_{\text{int}}\left(t = 0\right), \Pi_{\text{int}}\left(t = t^*\right)\right) \ , \tag{A.4}$$

$$\Pi_{\text{c}}^{\text{max}} = \max_{\forall\, t}\left(\Pi_{\text{c}}^{\text{rep}}, \Pi_{\text{c}}^{\text{adh}}\right) \ , \tag{A.5}$$

Based on the above definition, the following classification can be made as shown in Table A.1. It is pointed out that the factor 20 is chosen arbitrarily.

Acknowledgements

The authors are grateful to the German Research Foundation (DFG) for supporting this research under projects SA 1822/5-1 and GSC 111. The authors will also like to thank the reviewers for their helpful comments and suggestions.

Table A.1: Classification of a problem into adhesion or repulsion dominated problem.

S. No.	Condition	Contact classification
1.	$\Pi_c^{rep} > \Pi_c^{adh}$ and $\Pi_{int}^{max} < 20 \times \Pi_c^{max}$	impact dominated problem
2.	$\Pi_c^{rep} < \Pi_c^{adh}$ and $\Pi_{int}^{max} < 20 \times \Pi_c^{max}$	adhesion dominated problem
3.	$\Pi_{int}^{max} > 20 \times \Pi_c^{max}$	internal energy dominated problem

References

Bathe, K. J. (2007). Conserving energy and momentum in nonlinear dynamics. *Comput. Struct.*, 85:437–445.

Betsch, P. and Steinmann, P. (2001). Conserving properties of a time FE method-part II: Time-stepping schemes for non-linear elastodynamics. *Int. J. Numer. Meth. Engrg.*, 50:1931–1955.

Bravo, R., Pérez-Aparicio, J. L., and Laursen, T. A. (2011). An enhanced energy conserving time stepping algorithm for frictionless particle contacts. *Int. J. Numer. Meth. Engrg.*, 85:1415–1435.

Gonzalez, O. (1996). Time integration and discrete hamiltonian systems. *J. Nonlinear Sci.*, 6:449–467.

Hesch, C. and Betsch, P. (2009). A mortar method for energy-momentum conserving schemes in frictionless dynamic contact problems. *Int. J. Numer. Meth. Engrg.*, 77:1468–1500.

Hesch, C. and Betsch, P. (2010). Transient three-dimensional domain decomposition problems: Frame-indifferent mortar constraints and conserving integration. *Int. J. Numer. Meth. Engrg.*, 82:329–358.

Israelachvili, J. N. (1991). *Intermolecular and Surface Forces*. Academic Press, London.

Krenk, S. (2009). *Non-linear Modeling and Analysis of Solids and Structures*. Cambridge University Press, Cambridge.

Laursen, T. A. and Love, G. (2002). Improved implicit integrators for transient impact problems-geometric admissibility within the conserving framework. *Int. J. Numer. Meth. Engrg.*, 53:245–274.

Mohr, R., Menzel, A., and Steinmann, P. (2008). Galerkin-based mechanical integrators for finite elastodynamics formulated in principal stretches - Pitfalls and remedies. *Comput. Meth. Appl. Mech. Engrg.*, 197:4444–4466.

Newmark, N. N. (1959). A method for computation for structural dynamics. *Proc. of the ASCE: J. Eng. Mech. Division*, 85:67–94.

Ortiz, M. A. (1986). A note on energy conservation and stability of nonlinear time-stepping algorithms. *Comput. Struct.*, 24:167–168.

Sauer, R. A. (2006). *An atomic interaction-based continuum model for computational multiscale contact mechanics*. PhD thesis, University of California at Berkeley.

Sauer, R. A. (2009). Multiscale modelling and simulation of the deformation and adhesion of a single gecko seta. *Comput. Meth. Biomech. Biomed. Engrg.*, 12:627–640.

Sauer, R. A. (2011a). Challenges in computational nanoscale contact mechanics. In Mueller-Hoeppe, D., Loehnert, S., and Reese, S., editors, *Recent Developments and Innovative Applications in Computational Mechanics*, chapter 5, pages 39–46. Springer-Verlag, Heidelberg.

Sauer, R. A. (2011b). Enriched contact finite elements for stable peeling computations. *Int. J. Numer. Meth. Engrg.*, 87:593–616.

Sauer, R. A. and Li, S. (2007). A contact mechanics model for quasi-continua. *Int. J. Numer. Meth. Engrg.*, 71:931–962.

Sauer, R. A. and Lorenzis, L. D. (2012). A computational contact formulation based on surface potentials. *Comput. Meth. Appl. Mech. Engrg.* in press.

Sauer, R. A. and Wriggers, P. (2009). Formulation and analysis of a 3D finite element implementation for adhesive contact at the nanoscale. *Comput. Meth. Appl. Mech. Engrg.*, 198(49-52):3871–3883.

Simo, J. C. and Tarnow, N. (1992). The discrete energy-momentum method. conserving algorithms for nonlinear elastodynamics. *Z. Angew Math. Phys*, 43:757–792.

Wriggers, P. (2008). *Nonlinear Finite Element Methods*. Springer-Verlag, Heidelberg.

Xu, X. P. and Needleman, A. (1993). Void nucleation by inclusions debonding in a crystal matrix. *Model. Simul. Mater. Sci. Engrg.*, 1:111–132.

Zienkiewicz, O. C. and Taylor, R. L. (2005). *The Finite Element Method for Solid and Structural Mechanics*. Butterworth-Heinemann, Oxford, 6^{th} edition.